University of Padova

Department of Physics and Astronomy "Galileo Galilei"

Master Thesis in Astrophysics and Cosmology

Pair instability supernovae across cosmic time

Supervisor
Dr. Giuliano Iorio
University of Padova

Co-supervisor
Prof. Michela Mapelli
University of Heidelberg

Master Candidate
Raffaele Scala

Academic Year
2022-2023

Al mio papà

Abstract

Pair instability (PISNe) and pulsational pair instability supernovae (PPISNe) are a key to understand the final fate of massive stars. Despite the robust theoretical framework they are grounded in, we still do not have any uncontroversial detection of PISNe and PPISNe. The aim of this work is to investigate their event rate as a function of cosmic time, with particular focus on the effects of metallicity and binary evolution, and make a comparison with observational constraints. For this purpose, we use the population-synthesis code SEVN (Stellar EVolution for N-body) to produce catalogues of single and binary stellar populations. We feed these catalogues to the code COSMORATE, to evaluate the event rate density in cosmological epochs. From our simulations it appears that binary evolution is a key ingredient that enhances the rate of PISNe and PPISNe. We further speculate about a possible tension with observational constraints.

Contents

Listing of figures

Listing of tables

Listing of acronyms

VMS ..... Very massive star

PISN ..... Pair instability supernova

PPISN ..... Pulsational pair instability supernova

CCSN ..... Core collapse supernova

MW ..... Milky Way

LMC ..... Large Magellanic Cloud

BSS ..... Binary stellar systems

RLOF ..... Roche lobe overflow

MS ..... Main sequence

ZAMS ..... Zero-age main sequence

SSE ..... Single stellar evolution

BSE ..... Binary stellar evolution

WD ..... White dwarf

BH ..... Black hole

GW ..... Gravitational wave

SFR ..... Star formation rate

SFRD ..... Star formation rate density

SFH ..... Star formation history

IC ..... Initial condition

SSP ..... Single stellar population

BSP ..... Binary stellar population

1 Introduction

The thesis is organized as follows. In Chapter 2 we set the astrophysical basis for our work. We describe the processes through which pair-creation instability can take place in astrophysical context and for which kind of objects. Some possible candidates are mentioned and a framework for constraints on observability is arranged.
Chapter 3 describes the astrophysical relevance of binary stellar systems. Here we carry out a detailed description of how companion stars in these systems can interact and transfer their mass each other, sometimes in ways that can lead to merger events. This processes, typical of binary evolution, can drastically alter the evolutionary path of single stars, enhancing the probability of occurrence of pair instability processes within the system.
In Chapter 4, we introduce one of the main computational tools used for this thesis: the population synthesis code SEVN. Here we describe how SEVN can provide population synthesis resembling real stellar population. In particular we describe how it simulates evolutionary processes of single star, by means of interpolation of pre-computed stellar tracks, and binary evolution by means of analytic and semi-analytic methods.
In Chapter 5 we focus on the cosmological evolution of pair instability processes with respect to redshift. For this reason a detailed analysis of cosmic star formation rate and cosmic metallicity evolution is needed. Then we introduce the code COSMORATE. In Section 5.3 we describe how COSMORATE estimates the evolution of event rate densities – for the processes of pair creation instability – across cosmological epochs, interfacing data driven prescription for star formation and metallicity evolution with catalogs from population synthesis codes like SEVN.

Chapter 6 contains the results of all the simulations performed with SEVN, for different kind of populations, and the data analysis carried out for their outcome. The data from population synthesis have then been fed to COSMORATE. Concluding remarks and comparisons with observational constraints are eventually reported in Chapter 7.

2

Pair instability supernovae

In this chapter we describe the characteristics of very massive stars (VMSs, $M \gtrsim 100\,\mathrm{M}_\odot$) focusing on their final fates in a theoretical framework. We then analyse some possible candidates and the constraints for their observability.

2.1 Very massive stars and pair instability

Very massive stars are defined as stars with an initial mass larger than $100\mathrm{M}_\odot$. Because of this extreme mass, they experience different evolutionary stages, and in particular different final fate, with respect to lower massive stars ($10\mathrm{M}_\odot \lesssim M \lesssim 100\mathrm{M}_\odot$). These in fact, defined simply as massive stars, undergo a core collapse supernova (CCSN) in correspondence of iron burning in their cores. VMSs instead are expected to experience a pair-creation instability during their oxygen core-burning phase if they do not lose too much mass during their lives. This process brings them, in most of the cases, to end their lives even before the iron-core burning phase with a thermonuclear explosion.

For years the evolution of these stars was considered only in the framework of Population III stars. These are the first stars formed in the Universe, born from primordial nucleosynthesis material, and for this reasons lacking of heavy metals, so with metallicity $Z \sim 0$.

It is believed that first stars were intrinsically massive because of the lack of efficient coolants in the primordial gas. In fact, in this context, the main coolants for the collapse of primordial cloud – leading to the formation of Population III stars – are the H_2 molecules. The primordial

gas, as aforementioned, is deficient in heavy elements, which are the most efficient coolants in present-day star formation. Moreover the minimum mass at the onset of collapse is determined by the Jeans mass that scales with the temperature as $M_J \propto T^{\frac{3}{2}}$.
If H_2 is less efficient in cooling the primordial cloud, with respect to metals in present-day star formation, it can remain hot during the collapse. Considering this and the behaviour of M_J with the temperature, we expect that the collapse leads to the formation of very massive stars Population III stars. This result, in many cases, is validated by simulations, even if also other physical quantities assume a key role e.g. gas number density – see Abel et al. (2000, [1]), Nakamura & Umemura (2001, [2]), Bromm et al. (2009, [3]).
For what above-mentioned we expect Population III stars to be good candidate for VMSs. However, both observations and advanced stellar evolution models suggest that VMSs are also relevant in local Universe, at non-zero metallicity.
Furthermore, we are interested in metallicity because it is a fundamental quantity on which mass loss, due to stellar winds, depends. Vink et al. (2001, [4]) found that the mass loss rate vs. metallicity dependence behaves as a power-law with $\dot{M} \propto Z^{0.69}$ for O stars and $\dot{M} \propto Z^{0.64}$ for B supergiants. For this reason low metallicity stars avoid strong mass loss, remaining massive throughout all their lives. This can favor them to end up in the mass range in which pair instability can take place. Indees, as described by Woosley & Heger & Weaver (2002, [5]) the domain of pair instability supernovae is prescribed by the star helium-core mass M_{He}: if this is larger than $40 M_\odot$ an explosion powered by nuclear burning is possible.
After experiencing hydrogen, helium and carbon burning, the core temperature of these stars approaches 10^9K. At this point the whole star starts contracting at an accelerated rate. Energy from photons that might have gone into raising the temperature and providing more radiation pressure is instead diverted to the production of electron-positron pairs ($\gamma + \gamma \rightarrow e^- + e^+$). Regions in which this process happens become locally dynamically unstable. To check if a star is globally stable or not, a perturbation method should be adopted. However, Stothers (1999, [6]) showed that an evaluation of the first adiabatic exponent properly weighted and integrated over the whole star, $\langle \Gamma_1 \rangle$, is a very good approximation to determine the dynamical stability of a star. Therefore we adopted the Stothers (1999, [6]) stability criterion, which states that a star is stable if

$$\langle \Gamma_1 \rangle = \frac{\int_0^M \frac{\Gamma_1 P}{\rho} dm}{\int_0^M \frac{P}{\rho} dm} > \frac{4}{3}, \tag{2.1}$$

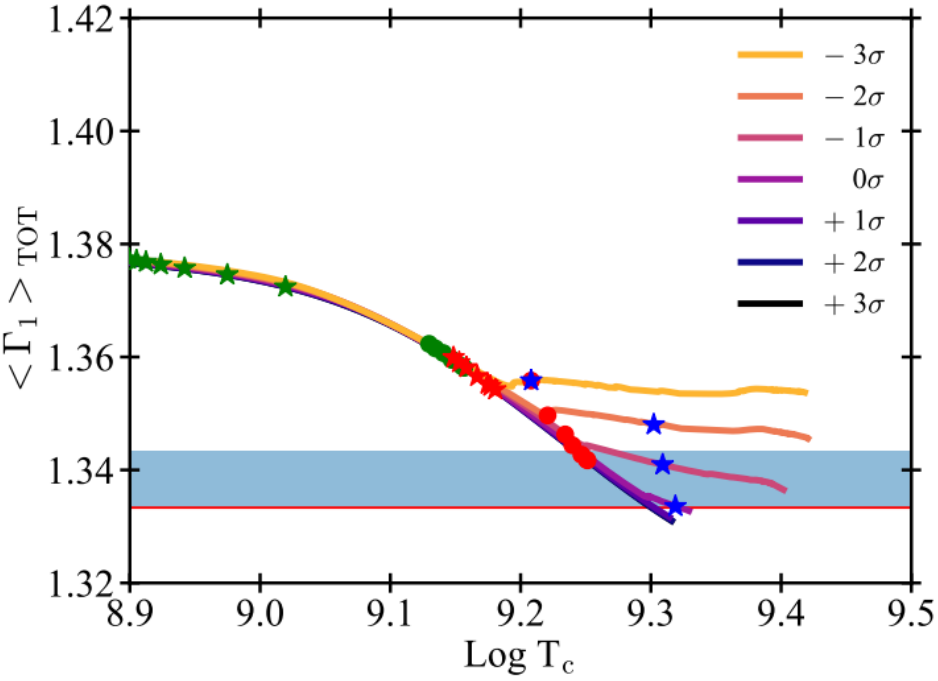

Figure 2.1: Comparison, made by Costa et al. (2020, [7]), of the averaged first adiabatic index $\langle\Gamma_1\rangle$ values versus the central temperature of stars with hydrogen envelopes and $M_{ZAMS} = 100\mathrm{M}_\odot$. They used seven different values of the multiplier parameter for the $^{12}C(\alpha,\gamma)\,^{16}O$ reaction rate, that correspond to varying the rate between -3σ and ¸$+3\sigma$. The lines corresponding to $+2$ and ¸3σ are barely visible, because they almost perfectly overlap with the ¸$+1\sigma$ line. The symbols indicate carbon (green), neon (red) and oxygen (blue) burning phases, respectively. Stars and circles symbols indicate the ignition and depletion of each element, respectively. The red horizontal line corresponds to $\langle\Gamma_1\rangle = 4/3$. The above blue shaded area indicates values between $4/3$ and $4/3+0.01$, range in which the whole star starts to be dynamically unstable.

where $\Gamma_1 = (\partial \ln P/\partial \ln \rho)_{\mathrm{ad}}$ is the first adiabatic exponent, P is the pressure, ρ is the density and dm is the element of mass.

When $\langle\Gamma_1\rangle < 4/3$ the star undergoes an instability. Indeed, radiation pressure is not able anymore to sustain the inward gravitational pull produced from the large mass of the star. In this case higher is the temperature, more pairs are produced and the implosion accelerates.

At this point, if the collapse velocity is not too high, the energy realised from subsequent nuclear reactions eventually halts the infall producing a bounce. The more massive is the helium core, the deeper the bounce, the higher the bounce temperature, and the greater the amount of oxygen burned. This process reverts the implosion in a thermonuclear explosion that totally disrupts the star.

Although this is the main mechanism for pair-creation instability, depending on the helium core mass, the situation can change. What we have just described as a single explosion unbind-

ing the star is called pair instability supernova (PISN) and occurs when the helium core mass is above $65\mathrm{M}_\odot$ and below $130\mathrm{M}_\odot$ (or main-sequence masses $\sim 140 - 260\mathrm{M}_\odot$ for $Z = 0$). Instead, for helium core mass between about $40\mathrm{M}_\odot$ and $65\mathrm{M}_\odot$, corresponding to main-sequence mass in the range $100 - 140\mathrm{M}_\odot$ for $Z = 0$, the pair instability leads to violent mass-ejecting pulsations and for this reason we talk about pulsational pair instability supernova (PPISN).
In the pulsational case, the energy released by the explosive burning is inadequate to unbind the entire star. It suffices, however, to violently eject several solar masses of surface material, including all that is left of the hydrogen envelope, in a series of giant pulses. After each pulse, the remaining core contracts, radiates neutrinos and light, and searches again for a stable burning state. The time required for this contraction is sensitive to the strength of the pulse and how close the star came to becoming unbound, producing an effective PISN. If the remaining helium core is still over 40 solar masses the star encounters the instability again, and ejects another several solar masses. Later ejections carry lower mass, because the envelope was expelled in the first pulse, but have higher energy. After several eruptions, when the helium core is not anymore over $40\mathrm{M}_\odot$, the star is not able to undergo pair instability anymore. From this point the star likely proceeds through the remaining nuclear burning steps up to the formation of the Fe core, analogously to massive stars. As them it eventually explodes as a CCSN leaving a neutron star or a black hole as a remnant [8].
If we instead consider higher initial stellar masses ($M > 260\mathrm{M}_\odot$) oxygen burning is inadequate to reverse the momentum of the implosion and the star can directly collapse into a black hole. With rotation, the mass limit for black hole formation increases and still more violent explosions can occur [5][9].

2.2 VMS observations

The field of very massive stars is in continuous development and in particular the observability of these objects is a hot topic in modern astrophysics. The existence of stars with masses $\gtrsim 10^2\mathrm{M}_\odot$ in the local universe in fact can challenge our stellar evolutionary models and undermine the upper mass limit for Kroupa initial mass function, usually set around $150\mathrm{M}_\odot$.
Nevertheless, in recent years we had some evidence for observations of very massive stars, e.g. Crowther et al. (2010, [10]). In this work they reported the observations of stars with mass larger then $100\mathrm{M}_\odot$ in R136, the central concentration of stars in the NGC 2070 star cluster (also known as Tarantula nebula or 30 Doradus) in the Large Magellanic Cloud, and in NGC 3603 a nebula situated in the Carina–Sagittarius Arm of the Milky Way.

Name	Current mass in $M_\odot$	Location
R136a1	265(320)	LMC
R136a2	195	LMC
R136c	175	LMC
Peony star (WR 102ka)	175 WR	MW
HD 269810	150	LMC
VFTS 682	150 WR	LMC
R136a3	135	LMC
NGC 3603-B	132	MW
Arches-F9	120 WN	MW
η Carina-A	120(160)	MW

Table 2.1: List of the most massive stars observed so far. The numbers in parentheses, following the current mass, stand for the estimated initial masses. WR, WN, MW and LMC mean respectively Wolf-Rayet star, Wolf-Rayet of type WN, Milky Way and Large Magellanic Cloud.

Through spectroscopic analyses using Hubble Space Telescope and Very Large Telescope and near infrared photometry, they derived important parameters for WN stars (a spectroscopic class of Wolf-Rayet stars) in these two systems. In particular, they found that these stars make a disproportionate contribution to the global ionizing and wind power budget of their host clusters. Indeed, the star R136a1 alone supplies $\sim 7\%$ of the ionizing flux of the entire 30 Doradus region. Comparisons with stellar models suggest ages of ~ 1.5 Myr and initial masses in the range $105 - 170 M_\odot$ for three systems in NGC 3603, plus $165 - 320 M_\odot$ for four stars in R136.

As this work, many others have identified very massive stars in the local universe, in particular in the Milky Way and in the Large Magellanic Cloud, as it is possible to see from Table 2.1 from Kozyreva (2014, [11]).

2.3 PISN CANDIDATES AND CONSTRAINTS

As discussed above, many present-day VMSs in their main evolutionary stages have been discovered and many of them greatly exceed $100 M_\odot$. Since these stars are thought to be progenitors of PISNe and PPISNe we expect that, within metal-poor environments, these supernovae can actually occur, even in the local universe. This is exactly what has been claimed for SN 2006GY by Smith et al. (2007, [12]) and SN 2007bi by Gal-Yam et al. (2009, [13]). In both cases we have different hints suggesting that these events actually correspond to PISNe.

Figure 2.2: The image shows the central region of the Tarantula Nebula in the Large Magellanic Cloud. The young and dense star cluster R136 can be seen on the right of the image.

For the case of SN 2006GY, Smith et al. (2007, [12]) observed a Type IIn supernova in NGC 1260 revealing that it reached a peak visual magnitude of about -22, making it, at the time of observation, the most luminous supernova ever recorded. It had a very slow rise to maximum that took about 70 days and stayed brighter than -21 mag for about 100 days. The estimated total radiated energy was $\sim 10^{51}$erg. For any known mechanism of production of energy – thermal emission, circumstellar interaction, or ^{56}Ni decay – such enormous energy would require a very massive progenitor star. Considering radioactive decay of ^{56}Ni, it would imply a large Ni mass of $\sim 22M_{\odot}$. This large presence of nickel could be a signature indicating that SN 2006gy was a PISN – see Kozyreva & Yoon & Langer (2021, [14]) – where the star's core was obliterated, or a PPISN, as claimed by Woosley & Blinnikov & Heger (2007, [8]). More in general the huge radiated luminosity, the long duration, the presence of hydrogen in the spectrum, the low expansion speed of the supernova ejecta are all consistent with the hypothesis that this event was powered by a pair-creation instability implying that, in this hypothesis, the progenitor star's initial mass may have been $\sim 150M_{\odot}$.
The case of SN 2007bi is quite different from the previous one. In fact spectroscopic observation showed no trace of either hydrogen or helium, leading to a Type Ic classification. The

measured light curve showed a very long rise time to peak of ~ 70 days, an extreme luminosity reaching an absolute peak R-band magnitude of $M_R = -21.3$ mag, and a slow decline of 500 days. These properties suggest that the very massive ejecta were energized, as probably also for the case of SN 2006GY, by a large amount of radioactive nickel ($> 3\mathrm{M}_\odot$) as expected from pair instability SN models. The large amount of kinetic energy released ($\sim 10^{53}$ erg) place this event among the most extreme explosions known. Moreover the data from the light curve fit very well the theoretical light curves calculated from PISN models. These data would suggest that the progenitor of the supernova was a very massive star with a helium core mass of around $100\mathrm{M}_\odot$. The quantitative estimate of the helium core mass and the analysis of the nebular spectra, is inconsistent with iron-core-collapse models, that so can be discarded, and theoretically requires a PISN. Is possible to conclude that most likely this represent the first clear example of a PISN.

2.3.1 Observational rates

Despite we have some observations resembling PISNe and PPSINe events – see Arcavi et al. (2017, [15]) – these results aren't at all satisfactory in a theoretical framework, where the relative event rate between CCSN and PISN should be $\sim 1\%$ from the conventional stellar evolution simulations for the Salpeter IMF [16]. In fact, thanks to the development of automated wide-field surveys, currently more than 1000 supernovae are discovered every year. This large number might be enough for the detection of PISNe. The above estimate of 1% for the relative event rate of PISNe to CCSNe is based on a conventional estimate for the initial mass range of PISNe found in section 2.1 of $140 - 260\mathrm{M}_\odot$.

A way to understand the possible origin of this discrepancy is provide by Takahashi (2018, [16]). Here is displayed the possibility that the event rate of PISNe has possibly been overestimated if the upper and lower ends of the PISN mass range have been underestimated. In fact most estimates of the PISN initial mass range assume the well-defined mass range of the carbon-oxygen (CO) core for PISNe of $\sim 65 - 120\mathrm{M}_\odot$ but this range could actually be shifted toward higher masses.

Investigating the evolution of VMSs with various core carbon-to-oxygen (X(C)/X(O)) ratios, they found that VMSs with high core carbon-to-oxygen ratios follow a qualitatively different evolutionary path from conventional models. In particular less massive VMSs avoid pair-creation instability since their effective core masses are reduced during the carbon-burning

phase by developing shell convection. While more massive models, still considering an high carbon-to-oxygen ratios, have an higher explodabilities, i.e. a star with high X(C)/X(O) explodes with a smaller explosion energy. Consequently, the initial mass range for PISNe increases increasing the carbon-to-oxygen ratio. This would cause PISNe to be much rarer (and fainter) of what previously thought.

The above-mentioned result would suggest a reduction of the relative rate between PPSINe and CCSNe. This is in agreement with what found by Moriya et al. (2021, [17]) that conducted a long-term survey using Hyper Suprime-Cam (HSC) on the 8.2m Subaru telescope, to constrain the rates of supernovae lasting more than a year (in which also PISN are included). Among all the long-lasting supernovae found (all likely Type IIn supernovae) no plausible PISN candidate has been discovered. Comparing these results with survey simulations is possible to constrain the pair instability supernovae rate for $z \lesssim 3$. In this way they discovered that the rate is of the order of 100 Gpc^{-3} yr^{-1} at most and the relative rate with core collapse supernovae is $0.01 - 0.1\%$, substantially lower than the above estimate of $\sim 1\%$.

3

Binary evolution

In this chapter we describe which are the main properties of binary stellar systems (BSS) and how their evolution can be relevant in the field of PISN and PPISN formation.

3.1 Binary properties

Most stars in the sky are in binary systems or, more generally, in multiple systems. Of course, the majority of binaries are in fairly wide systems that do not interact strongly and where both stars evolve essentially as single stars. But there is a large fraction of systems (with orbital period $P_{\rm orb} \lesssim 10$yr) that are close enough that mass is transferred from one star to the other changing the structures of both stars and their subsequent evolution [18]. Binary surveys suggest that the range of interacting binaries, which are the systems of interest in this chapter, is in the range of 30% to 50% where the binary fraction is higher for more massive stars; see e.g. Duquennoy & Mayor(1991, [19]), Kobulnicky & Fryer(2007, [20]).
The most important parameters for the description of binary systems are the mass-ratio distribution i.e. $q = M_1/M_2$, where M_1 and M_2 are the initially more massive (the primary) and the initially less massive star (the secondary) respectively, and the already cited orbital period $P_{\rm orb}$, that can range from 11 min (for a NS-WD binary) to $\sim 10^6$ yr .

3.2 Mass transfer

If two stars exchange matter to each other, it means they undergo a mass transfer episode. This might be driven either by stellar winds or by an episode of Roche lobe filling.
When a massive star loses mass by stellar winds, its companion might be able to capture some of this mass. This will depend on the amount of mass which is lost and on the relative velocity of the wind with respect to the companion star. Since the mass loss rate of the donor is usually quite low ($\dot{M}_1 < 10^{-3}\,\mathrm{M}_\odot\,\mathrm{yr}^{-1}$) and because of the geometry of the system this kind of mass transfer is usually quite inefficient.
Roche lobe, instead, is a key concept for mass transfer and the evolution of binary systems. Considering the so called restricted three body problem, where one follows the motion of a mass-less test particle in the gravitational field of two orbiting masses M_1 and M_2, one can define an effective potential in a co-rotating frame that includes the gravitational potential of the two stars and the centrifugal force acting on the test particle (this assumes that the orbit is circular). This potential has 5 so-called Lagrangian points where the gradient of the effective potential is zero (i.e., where the net force is 0 in the co-rotating frame). The three most important ones lie along the line that connects the two stars. Of particular importance is the inner one, referred to as L1 or inner Lagrangian point, since the equipotential surface that passes through this point connects the gravitational spheres of influence of the two stars. This means that, if one star starts to fill its Roche lobe (the teardrop-shaped equipotential surface surrounding each star), then matter can flow through the L1 point into the Roche lobe of the other star. This is the most efficient way of how mass can be transferred from one star to the other and it is called Roche lobe overflow (RLOF). The effective Roche lobe radius R_L only depends on the orbital separation a and the mass-ratio q. For circular orbits and primary star with mass M_1, it is well approximated by the following expression from by Eggleton (1983, [21])

$$R_L = \frac{0.49q^{-\frac{2}{3}}}{0.6q^{-\frac{2}{3}} + \ln(1+q^{-\frac{1}{3}})}a, \tag{3.1}$$

and an analogous expression holds for the effective Roche lobe radius of secondary star .
Mass transfer obviously changes the mass of the two stars in a binary, and thus the orbital properties of the binary. But since the mass is a parameter regulating the evolutionary path of stars, a variation in mass due to mass transfer will impact on subsequent evolutionary stages and also on the final fates of stars. For these reasons the study of mass transfer is of fundamental im-

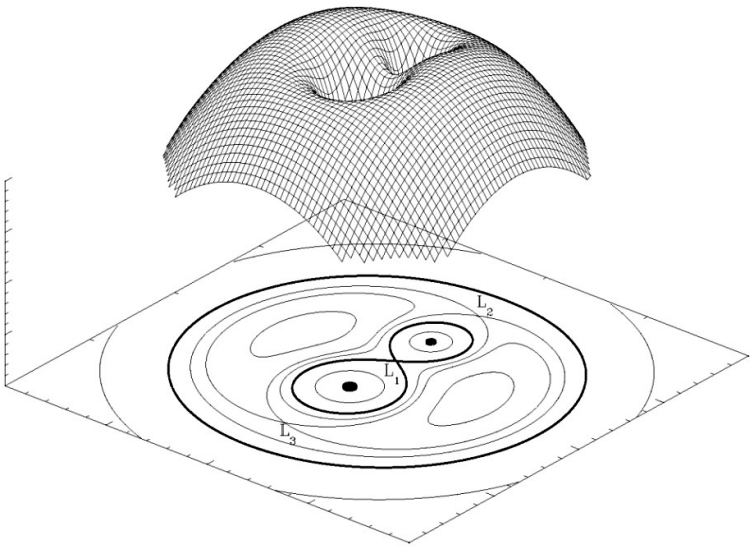

Figure 3.1: In this image is possible to see the equipotential surface of Roche lobe potential and the equipotential lines, projected on the orbital plane, with the position of three Lagrangian points L1, L2 and L3

portance when dealing with the evolution of VMSs and pair-creation instability. Through this process, as we are going to see in the next section, stars can gain mass or even merge undertaking a totally different evolutionary path, giving birth to objects that, because of their increased mass, could more likely find themselves in the mass range – discussed in chapter 2 – of PISNe or PPISNe.

3.3 Roche lobe overflow

A crucial information about Roche lobe overflow is whether it is stable or unstable. For what concerns the stable case, it is the easiest type of mass transfer to understand. In this case, most, but not necessarily all, of the transferred mass is accreted by the companion star, generally leading to a widening of the binary. Mass transfer ends when the donor star does not fill its Roche lobe anymore or most of its hydrogen-rich envelope has either been transferred to the companion or been lost from the system. In the latter cases, the end product will be a hydrogen-exhausted helium star with at most a small hydrogen-rich envelope [22]. Mass accretion will also change the structure of the accreting star. If it is still on the main sequence, the accretor tends to be rejuvenated and then behave like a more massive normal main-sequence star.
The most used approach to better describe RLOF and to discriminate if it is stable or not is

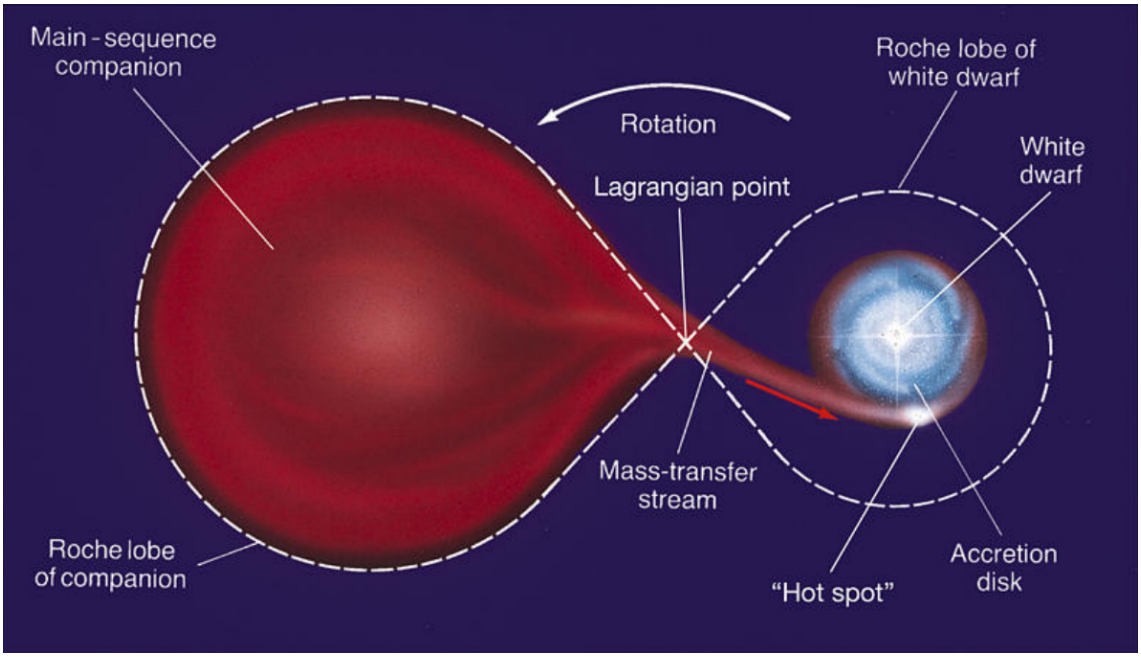

Figure 3.2: Roche lobe overflow between a main-sequence star and an accreting white dwarf. In this case the mass streaming from the companion to the white dwarf lead to the formation of an accretion disk.

the following [23]. Let us assume that the stellar radius and mass are connected by a simple relation $R \propto M^{\zeta}$. Thus, the variation of the donor's radius during Roche lobe is

$$\frac{dR_1}{dt} = \frac{\partial R_1}{\partial t} + \zeta \frac{R_1}{M_1} \frac{dM1}{dt}. \tag{3.2}$$

In the above equation, the term $\frac{\partial R_1}{\partial t}$ is due to nuclear burning, while the term with ζ measures the adiabatic or thermal response of the donor star to mass loss. Note that $\frac{dM1}{dt}$ is the mass loss from the donor; hence it is always negative.
Similarly, the change of the size of the Roche lobe of the donor R_L can be estimated as

$$\frac{dR_{L,1}}{dt} = \frac{\partial R_{L,1}}{\partial t} + \zeta_L \frac{R_{L,1}}{M_1} \frac{dM1}{dt} \tag{3.3}$$

where $\frac{\partial R_{L,1}}{\partial t}$ depends on tides and GW radiation, while ζ_L describes the response of the Roche lobe to mass loss: the Roche lobe might shrink or expand. If $\zeta_L > \zeta$, the Roche lobe shrinks faster than the radius of the star does and the mass transfer is unstable, otherwise it remains stable until the radius changes significantly by nuclear burning.

In the context of mass transfer two timescales have an important role concerning the response of the donor star to mass loss. They are the dynamical timescale

$$t_{dyn} \sim \sqrt{\frac{\frac{4}{3}\pi R^3}{GM}} \sim 3300s \left(\frac{R}{R_\odot}\right)^{3/2} \left(\frac{\mathrm{M}_\odot}{M}\right)^{1/2} \tag{3.4}$$

that is the timescale for a star to collapse by its own gravity in absence of pressure, and the thermal, or Kelvin-Helmoltz, timescale

$$t_{KH} \sim \frac{GM^2}{RL} \sim 3 \times 10^7 yr \left(\frac{M}{\mathrm{M}_\odot}\right)^2 \frac{L_{odot}}{L} \frac{R_\odot}{R} \tag{3.5}$$

that is the timescale for a star to contract by radiating away all its gravitational potential energy. Mass transfer can be unstable either on one or on the other timescale. In particular if it is unstable on dynamical timescale, it means that ζ describes the adiabatic response of the donor to mass loss while, if it is unstable on thermal timescale, it means that ζ describes the thermal response of the donor; in both cases the condition for instability is $\zeta_L < \zeta$. If mass transfer is dynamically unstable or both stars overfill their Roche lobe, then the binary is expected to merge –- if the donor lacks a steep density gradient between the core and the envelope –- or to enter common envelope (CE) –- if the donor has a clear distinction between core and envelope.

Common envelope

If two stars enter CE, their envelopes stop co-rotating with their cores. The two stellar cores (or the compact object and the core of the companion star, if the binary is already single degenerate) are embedded in the same non-corotating envelope and start spiralling-in as an effect of gas drag exerted by the envelope. Part of the orbital energy lost by the cores as an effect of this drag is likely converted into heating of the envelope, making it more loosely bound. If this process leads to the ejection of the envelope, then the binary survives, but the post-CE binary is composed of two naked stellar cores (or of a compact object and a naked stellar core). Moreover, the orbital separation of the two cores is considerably smaller than the initial orbital separation before the CE, as an effect of the spiral-in. In contrast, if the envelope is not ejected, the two cores spiral in till they eventually merge. After the merger, the remnant will be a rapidly rotating super-giant star. In general, binary mergers can occur on a large range of timescales. This depends mainly on the structure of the envelope, in particular the density profile, since this

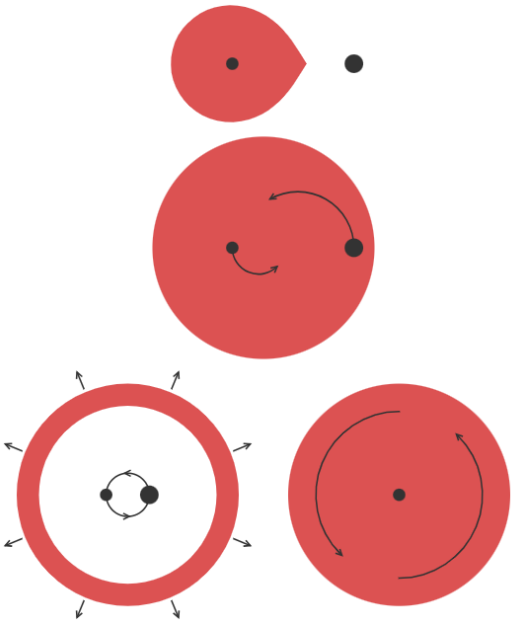

Figure 3.3: Key stages in the common envelope phase. In the first phase a star fill its Roche lobe and RLOF starts. Then the companion is engulfed in the envelope and both stars start to spiral-in. Eventually the envelope can be either ejected or the two stars can merge.

determines the friction timescale and hence the spiral in timescale during the spiral in phase. The different stages of CE phase are shown in Figure 3.3.

The α formalism is the most common formalism adopted to describe common envelope, even if the simplest one. It can gives us information on whether the binary merges or not during CE phase. The basic idea of this formalism is that the energy needed to unbind the envelope comes uniquely from the loss of orbital energy of the two cores during the spiral in. The fraction of the orbital energy of the two cores which goes into unbinding the envelope can be expressed as

$$\Delta E = \alpha(E_{b,f} - E_{b,i}) = \alpha \frac{GM_{c1}M_{c2}}{2}\left(\frac{1}{a_f} - \frac{1}{a_i}\right) \tag{3.6}$$

where $E_{b,i}$ ($E_{b,c}$) is the orbital binding energy of the two cores before (after) the CE phase, a_i (a_f) is the semi-major axis before (after) the CE phase, M_{c1} and M_{c2} are the masses of the two cores, and α is a dimensionless parameter that measures which fraction of the removed orbital energy is transferred to the envelope.

The binding energy of the envelope is

$$E_{env} = G\left[\frac{M_{env,1}M_1}{\lambda_1 R_1} + \frac{M_{env,2}M_2}{\lambda_2 R_2}\right], \tag{3.7}$$

where M_1 and M_2 are the masses of the primary and the secondary star of the binary, $M_{env,1}$ and $M_{env,2}$ are the masses of the envelope of the primary and the secondary star of the binary, R_1 and R_2 are the radii of the primary and the secondary star of the binary, and λ_1 and λ_2 are the parameters (or the functions) that measure the concentration of the envelopes of the stars (the smaller they are, the more concentrated are the envelopes).
By imposing $\Delta E = E_{env}$ we can derive the value of the final semi-major axis a_f for which the envelope is ejected. This means that the larger (smaller) α is, the larger (smaller) the final orbital separation. If the resulting a_f is lower than the sum of the radii of the two cores (or than the sum of the Roche lobe radii of the cores), then the binary will merge during CE, otherwise the binary survives.
Actually, we have known for a long time that this simple formalism is a poor description of the physics of CE, which is considerably more complicated. A lot of effort has been put in modelling the physics of CE with analytic models and numerical simulations, but still the problem remains largely unconquered [18][23].

The importance of binary interactions

We have just seen that in a binary system, the evolutionary path is drastically altered by the presence of a nearby companion because of mass exchange or even merger events. On top of this, we can also state that the frequency of interaction events within binaries, especially for massive stars, is quite high as revealed by Sana et al. (2012, [24]). Through the spectroscopic observation of O-type star (hot, blue-white star, typically very massive) population of six nearby Galactic open stellar clusters, they found that 71% of them interact with a companion, over half of which doing so before leaving the main sequence. Based on calculations of binary evolution in short-period systems, they also found that 20 to 30% of all O stars will merge with their companion, and that 40 to 50% will be either stripped of their envelope or will accrete substantial mass. Since also observations can confirm it, we can claim that binary interactions drastically alter the evolution and final fates of stars and is, by far, the most frequent evolutionary channel for more massive stars.

4

Population synthesis codes and SEVN

4.1 Population synthesis codes

Stellar population synthesis codes are designed to find a combination of stars producing the characteristics of a particular stellar population. By means of these codes, we are able to perform semi-analytic evolution of single and binary stellar populations, providing very large statistics. This aspect is of fundamental importance for us since the the parameters in which we are interested, regarding PISNe and PPISNe, must be statistically relevant.
To achieve this goal many simplifications are needed. In particular the overall hydrodynamical evolution of the systems, that would provide the highest possible accuracy, is not considered. It would require $\sim$ 1 million CPU hours for a single binary system. From this point of view binary population synthesis codes are certainly the fastest approach to model binary star evolution, from the zero-age main sequence (ZAMS) to the final fate. For example, the famous BSE code [25][26], which is the common ancestor of most binary population synthesis codes, evolves $\mathcal{O}(10^6)$ binary stars in a couple of hours on a single CPU core. For comparison, a modern stellar evolution code requires $\mathcal{O}(10 - 100)$ CPU hours to integrate the evolution of an individual binary star. The speed of binary population synthesis codes is essential not only to model the parameter space of massive binary star evolution, but also to guarantee that they can be interfaced with dynamical codes to study the dynamical formation of binary compact objects in dense stellar clusters [27].

A large number of binary population synthesis codes have been developed across the years. All of them are independent codes but, most of them rely on the same model of stellar evolution: the accurate and computationally efficient fitting formulas developed by Hurley et al. (2000, [25]), based on the stellar tracks by Pols et al. (1998, [28]). These fitting formulas express the main stellar evolution properties (e.g., photospheric radius, core mass, core radius, luminosity) as a function of stellar age, mass (M), and metallicity (Z). In this way the results of binary population synthesis codes adopting such fitting formulas can differ just by the way they model stellar winds, compact-remnant formation and binary evolution, but rely on the same stellar evolution model. This implies that they can probe only a small portion of the parameter space, that depends on the physics encoded in the original tracks by Pols et al. (1998, [28]). Moreover stellar evolution models changed a lot since 1998, also probing a much wider mass and metallicity range than the ones considered by Hurley et al. (2000, [25]).
In the years, alternative strategies have been developed to include, in new population synthesis codes, up-to-date stellar evolution and a wider range of masses and metallicities. These consist for example in integrating stellar evolution on the fly, e.g. BPASS (Eldridge et al., 2016, [29]); MESA (Paxton et al., 2011, [30]) or in reading stellar evolution from lookup tables. Among these we have codes like COMBINE (Kruckow et al., 2018, [31]), METISSE (Agrawal et al., 2020, [32]), POSYDON (Fragos et al., 2023, [33]) and SEVN (Spera et al., 2015, [34]; Spera & Mapelli, 2017, [35]; Spera et al., 2019, [36]; Iorio et al., 2023, [27]). They all share the same approach to stellar evolution that consists into including an algorithm that interpolates the main stellar-evolution properties (mass, radius, core mass and radius, luminosity, etc as a function of time and metallicity) from a number of pre-computed tables. The main advantage is that the interpolation algorithm is more flexible than the fitting formulas, in fact in order to update the stellar evolution model it is sufficient to generate new tables. Furthermore, this approach allows to easily compare different stellar-evolution models encoding different physics.
In this work we have used SEVN to explore the main properties and formation rates of PISNe and PPISNe both in single and binary stellar systems. For this reason we now describe the main characteristics of the code referring mainly to Iorio et al. (2023, [27]).

4.2 Description of SEVN

SEVN (Stellar EVolution for N-body) is a rapid binary population synthesis code, which calculates stellar evolution by interpolating pre-computed sets of stellar tracks [34] [35] [36]. Binary evolution is implemented through analytic and semi-analytic prescriptions. The main advan-

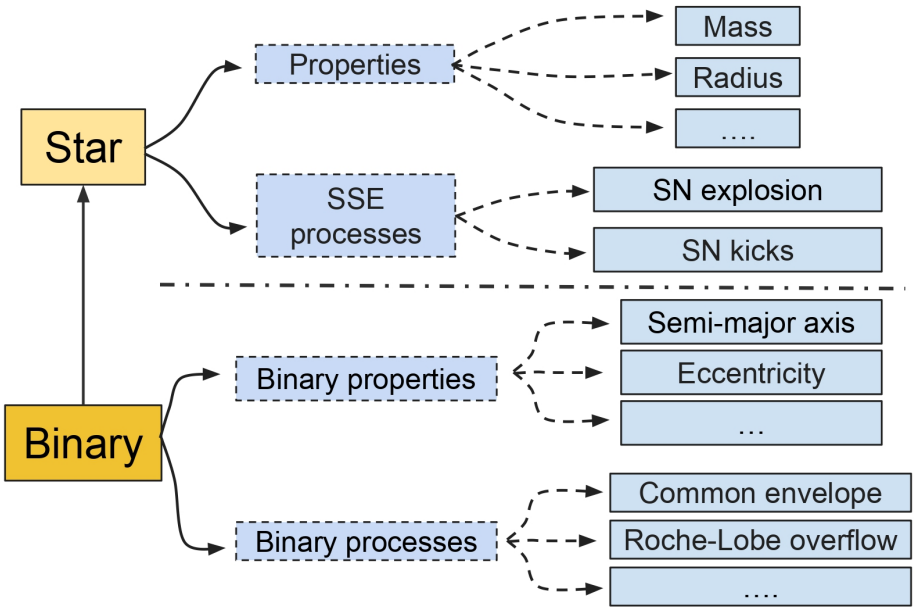

Figure 4.1: Single stars are characterised by their properties (mass, radius,...) and single stellar evolution processes (supernova explosion type and natal kicks). Binary stars are characterised by their properties (semi-major axis, eccentricity,..), binary-evolution processes (mass transfer by winds, Roche-lobe overflow, CE, tides,..), and by the two stars component of the binary system.

tage of this strategy is that it makes the implementation more general and flexible, in fact the stellar evolution models adopted in SEVN can easily be changed or updated just by loading a new set of lookup tables. SEVN allows to choose the stellar tables at runtime, without modifying the internal structure of the code or even recompiling it.
It is written completely in C++ and exploits the CPU-parallelisation through OpenMP. Single stars, binary systems, properties and processes are represented with C++ classes as it is possible to see from Figure 4.1

4.2.1 Single stellar evolution

The single stellar evolution (SSE) of a star is uniquely defined by two values: M_{ZAMS} and Z, i.e. the zero-age main sequence mass and its metallicity. For each couple of (M_{ZAMS}, Z) the SSE will be always the same (for a given set of evolutionary tracks). SEVN requires as input two sets of tables: one for stars starting their lives from hydrogen main sequence and the other for pure helium stars (stars that are H depleted).

For each stellar evolution model are needed at least seven mandatory tables, grouped by metallicity. Each table refers to a different stellar property. The seven mandatory tables correspond to the main stellar properties: time, total stellar mass, He-core mass, CO-core mass, stellar radius, bolometric luminosity, and the stellar phase. Additional properties such as the radii of the He and CO cores, the envelope binding energy and the properties of the convective envelope are optional. These tables are not mandatory because they contain information that are not available in most stellar-evolution tracks, but they are needed to properly model several evolution processes. The modular structure of SEVN makes it possible to easily introduce new tables to follow the evolution of additional stellar properties.

Stellar phases

Spera et al. (2019, [36]) found that the interpolation of stellar evolution properties significantly improves if we use the percentage of life of a star instead of the absolute value of its lifetime. In order to refine the interpolation, they estimated the percentage of life in three stellar macro-phases. Instead in the current, updated version of SEVN the stellar evolution is divided in seven physically motivated macro-phases. The first is the pre-main sequence phase, from the zero age to the start of ignition of hydrogen in the core (PMS, phase id = 0). During the hydrogen burning, the star is in the main sequence phase (MS, phase id = 1) until we have the creation of helium core and the star enters the terminal main sequence phase (TAMS, phase id = 2). In the next phase the hydrogen in the core has been completely exhausted and the star only burns hydrogen in the shell surrounding the helium core (SHB, phase id = 3). The star then starts burning helium in the core (CHeB, phase id = 4) and when the carbon-oxygen core starts to form we enter in terminal-age core He burning (TCHeB, phase id = 5, CO-core mass > 0) and in the shell helium burning (SHeB, phase id = 6) when helium has been exhausted in the core. The remnant phase (phase id = 7) begins when the evolution time exceeds the star's lifetime and the star becomes a compact remnant.

During its evolution, a star can be stripped of its hydrogen envelope either because of effective stellar winds or due to binary interactions. If the He-core mass is larger than 97.9% of the total stellar mass, SEVN classifies the star as a Wolf-Rayet (WR) star and the star jumps to a new interpolating track (see 4.2.3) on the pure-He tables. In SEVN, pure-He stars are not inscribed in a special phase, in fact the only difference with respect to hydrogen-rich stars is that a pure-He star does not go through phases $0-3$, but rather starts its life directly from phase 4 (CHeB).

In SEVN the properties of each star are estimated, at a given time, through interpolation. For each couple of (M_{ZAMS}, Z) that we want to calculate, SEVN assigns four interpolating tracks from the hydrogen or pure-He lookup tables. These tracks have two different metallicities (Z_1, Z_2) and four different ZAMS masses, two per each metallicity ($M_{ZAMS,1}$, $M_{ZAMS,2}$, $M_{ZAMS,3}$, $M_{ZAMS,4}$). These values are chosen as $M_{ZAMS,1/3} \leq M_{ZAMS} \leq M_{ZAMS,2/4}$ and $Z_1 \leq Z \leq Z_2$. A given interpolated property W is estimated as follows:

$$W = \frac{Z_2 - Z}{Z_2 - Z_1} W_{Z,1} + \frac{Z - Z_1}{Z_2 - Z_1} W_{Z,2} \tag{4.1}$$

where

$$W_{Z,1} = \beta_1 W_{ZAMS,1} + \beta_2 W_{ZAMS,2} \tag{4.2a}$$

$$W_{Z,2} = \beta_3 W_{ZAMS,3} + \beta_4 W_{ZAMS,4} \tag{4.2b}$$

In Eq. 4.2 $W_{ZAMS,i}$ indicates the value of the property W in the interpolating tracks with $M_{ZAMS,i}$ and β are interpolation weights. These weights can be either linear, logarithmic or rational depending on the interpolated property we are dealing with; see Iorio et al. (2023,[27]). When a star is initialised, SEVN uses the equations for interpolation 4.1 and 4.2 to set the starting times of the stellar phases ($t_{start,p}$) where in this case $W_{ZAMS,i}$ are the phase times.
Stellar lifetime is interpolated in the same way, assuming that the last element in the SEVN time table sets stellar lifetime. For all the other properties, W has to be estimated at a given time t. The corresponding $W_{ZAMS,i}$ in the tables is not estimated at the same absolute time t, rather at the same percentage of life in the phase of the interpolated star

$$\Theta_p = \frac{t - t_{start,p}}{t_{start,p_{next}} - t_{start,p}}, \tag{4.3}$$

where $t_{start,p}$ indicates the starting time of the phase p, and $t_{start,p_{next}}$ the starting time of the next phase p_{next}, obtaining in this way the phase time interval at the denominator. Hence, SEVN uses Eq. 4.3 to evaluate the times for each of the four interpolating tracks

$$t_i = t_{start,p,i} + \Theta_p \Delta_{p,i} \tag{4.4}$$

where $t_{start,p,i}$ and $\Theta_p\Delta_{p,i}$ are the starting time and the time duration of the current phase for each interpolating track, respectively. Once evaluated the time it can estimates $W_{ZAMS,i}$ in Eq. 4.2 by linear interpolation, along the time, of the values stored in the tables.
This division into phases guarantees that all the stars have the same internal structure reducing the interpolation error.

Compact remnants

A compact remnant forms when the evolution time exceeds the stellar lifetime. Depending on the final mass of the CO core, SEVN can trigger the formation of a white dwarf if the final CO mass is $M_{CO,f} < 1.38\mathrm{M}_\odot$, the explosion of an electron capture supernova ($1.38\mathrm{M}_\odot \leq M_{CO,f} < 1.44\mathrm{M}_\odot$) producing a neutron star, or a core collapse supernova ($M_{CO,f} \geq 1.44\mathrm{M}_\odot$). For our work is interesting to see the approach used in SEVN to handle pair-creation instability. In the updated version of the code are included two models for PPISNe and PISNe: M20 and F19. M20 – the model used to perform our simulations (see Chapter 6) – is based on the fit by Spera & Mapelli (2017, [35]) to the black hole (BH) mass obtained with 1D hydrodynamical simulations by Woosley (2017, [37]). Here a star undergoes PPISN if the pre-supernova He-core mass is within 32 and $64\mathrm{M}_\odot$, while a PISN is triggered for $64 \leq M_{He,f} \leq 135$ and above $135\mathrm{M}_\odot$ the star directly collapse to a BH, leaving an intermediate-mass BH.
PISNe leave no compact remnant, while the final mass of the compact remnant after PPISN is obtained by applying a correction to the BH mass predicted by the adopted core collapse supernova model M_{CCSN}. In this work we used just two core collapse models: the delayed and the rapid model by Fryer et al. (2012, [38]). These two only differ by the time in which the shock in CCSN is revived: < 250 ms and > 500 ms for rapid and delayed model, respectively. The mass of the PPISN remnant so is

$$M_{PPSIN} = \begin{cases} \alpha_P M_{CCSN} & \text{if } \alpha_P M_{CCSN} \geq 4.5\mathrm{M}_\odot \\ 0 & \text{if } \alpha_P M_{CCSN} \leq 4.5\mathrm{M}_\odot \end{cases} \tag{4.5}$$

The correction factor α_P depends on $M_{He,f}$ and the pre-supernova mass ratio between the mass of the He core and the total stellar mass and it can take any value between 0 and 1 (a value of 0 corresponds to a PISN). If $\alpha_P M_{CCSN} \leq 4.5\mathrm{M}_\odot$, a PISN is triggered and the mass of the compact remnant is set to zero. The limit at $4.5\mathrm{M}_\odot$ is based on the least massive BH formed in the simulations by Woosley (2017, [37]).

4.2.2 Binary evolution

SEVN performs binary stellar evolution by means of analytic and semi-analytic methods implemented to simplify a number of complex physical processes. They are wind mass transfer, RLOF, CE, stellar tides, circularisation at the RLOF onset, collision at periastron, orbit decay by gravitational waves (GWs) emission and stellar mergers. We now briefly describe how them are implemented in the code.

Wind mass transfer is implemented following the implementation used by Hurley et al. (2002, [26]), in which the orbit-averaged accretion rate is estimated according to Bondi & Hoyle (1944, [39]) mechanism and fast wind approximation (wind velocity faster then orbital velocity).

Then we have the Roche lobe overflow (RLOF) that in SEVN begins whenever the radius of one of the two stars becomes equal to (or larger than) R_L of Eq. 3.1, and stops when this condition is not satisfied anymore, or if the mass transfer leads to a merger or a CE. SEVN checks for this condition at every time-step. The RLOF implementation used in this work is based on Hurley et al. (2002 , [26]), Spera et al. (2019, [36]) and Bouffanais et al. (2021, [40]).

The CE evolution, as implemented in SEVN, is based on the so-called energy formalism as described in Hurley et al. (2002, [26]) and briefly mentioned in Section 3.3. This formalism is based on the comparison between the energy needed to unbind the stellar envelopes and the orbital energy before and after the CE event.

For what concerns tidal forces between two stars in a binary system, they tend to synchronise the stellar and orbital rotation, and circularise the orbit. In SEVN, the effect of tides on the orbit and stellar rotation follow the weak friction analytic models by Hut (1981, [41]), as implemented in Hurley et al. (2002, [26]). The model is based on the spin-orbit coupling caused by the misalignment of the tidal bulges in a star and the perturbing potential generated by the companion.

SEVN then describes the impact of GW emission on the orbital elements by including the same formalism as BSE code (Hurley et al. 2002, [26]):

$$\dot{a} = -\frac{64G^3 M_1 M_2 (M1+M2)}{5c^5 a^3 \left(1-e^2\right)^{\left(\frac{7}{2}\right)}} \left(1 + \frac{73}{24}e^2 + \frac{37}{96}e^4\right) \tag{4.6}$$

$$\dot{e} = -\frac{304G^3 M_1 M_2 (M1+M2)}{15c^5 a^4 \left(1-e^2\right)^{\left(\frac{5}{2}\right)}} \left(1 + \frac{121}{304}e^2\right) e. \tag{4.7}$$

The above equations, described in Peters (1964, [42]), account for orbital decay and circularisation by GWs. In SEVN they are switched on whenever the GW merger timescale, t_{merge}, is

shorter than the Hubble time. The GW merger timescale is estimated using a high-precision approximation of the solution of the systems of equations 4.6 and 4.7 – see Appendix D in Iorio et al. (2023, [27]).
Finally we have stellar mergers that have a strong impact in the field of PISNe and PPISNe formation (see Chapter 6). When two stars merge, SEVN simply sum their CO cores, He cores and total masses. The merger product inherits the phase and percentage of life of the most evolved progenitor star. The most evolved star is the one with the largest SEVN phase ID or with the largest life percentage if the merging stars are in the same phase.
In SEVN, we do not need to define a collision table for the merger between two stars because the interpolation algorithm finds the new post-merger track self-consistently, without the need to define a stellar type for the merger product. It makes instead use of a collision table when describing the outcome of mergers involving compact objects – see Table 4 in Iorio et al. (2023, [27]).

4.2.3 Evolution algorithm

Adaptive time-step and temporal evolution

SEVN uses a prediction-correction method to adapt the time-step accounting for the large physical range of timescales (from a few minutes to several Gyr) typical of stellar and binary evolution.
To decide the time-step, we look at a sub-set of stellar and binary properties (total mass, radius, mass of the He and CO core, semi-major axis, eccentricity, and amount of mass loss during a RLOF) and if any of them changes too much during a time-step, the time-step is reduced and the calculation repeated. What we do in practice is to choose a maximum relative variation δ_{max} (by default 0.05) and impose that

$$\max_{P \in properties} |\delta P| \leq \delta_{max}, \tag{4.8}$$

where $|\delta P|$ is the absolute value of the relative property variation.
SEVN then predicts the next time-step as

$$dt_{next} = \min_{P \in properties} \left(\delta_{max} \frac{dt_{last}}{|\delta P_{last}|} \right) \tag{4.9}$$

where dt_{last} is the last time-step and δP_{last} is the relative variation of property P during the last time-step, hence $\delta P_{last}/dt_{last}$ represents the absolute value of δP_{last} time derivative.

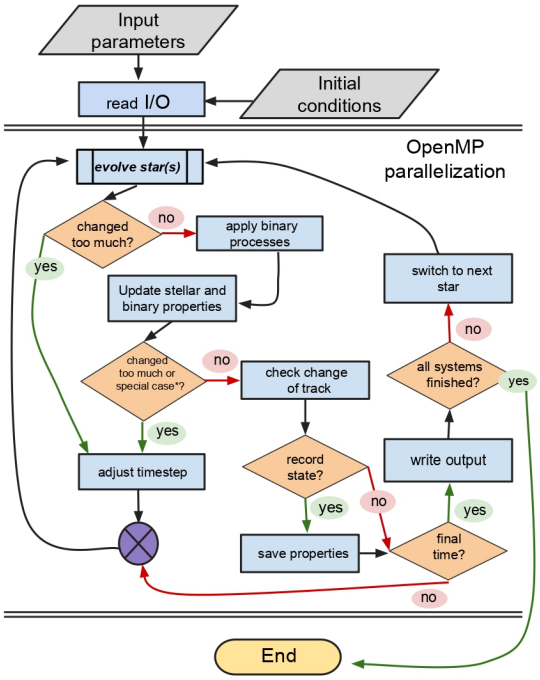

Figure 4.2: Schematic representation of the sevn evolution algorithm. The "changed too much" checks refer to the variation of the stellar and/or binary properties. In the case of single-stellar evolution or in the case of an ionized binary, sevn skips the sections "apply binary processes" and "update stellar and binary properties". The "special case" check refers to all the cases in which SEVN repeats the evolution to follow a particular binary evolution process, i.e, CE, merger, and circularistaion at the onset of the RLOF

After the evolution step (that we are going to see after), if the condition in Eq. 4.8 is not satisfied, a new smaller time-step is predicted using Eq. 4.9 and the updated values of δP_{last} and dt_{last}. Then, we repeat the evolution of all the properties with the new time-step until condition 4.8 is satisfied or until the previous and the new proposed time steps differ by less than 20%.

In the case in which a star approaches a change of phase, SEVN uses a different treatment. If the time-step is large enough to cross the time boundary between two phases, it is automatically reduced so that the next evolution step is brought to 10^{-10} Myr before the phase change. The next time-step, instead, is set such that it brings the star/binary 10^{-10} Myr beyond the phase change. In this way stellar properties are evaluated just before and after the phase change.

When evolving the systems,in each time-step, SEVN firstly evolves the two stars independently and after evaluates the accumulated property variation ΔP due to each binary evolution process. After the evaluation of the binary process, SEVN updates each stellar and binary property. In particular each binary property is evaluated as $P(t) = P(t_0) + \Delta P$, where $P(t_0)$ are the orbital and stellar properties at the beginning of the evolution step. Each single stellar evolution property is instead calculated as $P(t) = P_s(t) + \Delta P$, where $P_s(t)$ is the value of the property at the end of the time-step as predicted by single stellar evolution only. For example, if the property $P(t)$ is the mass of an accretor star during RLOF, $P_s(t)$ is the mass predicted at the end of the time-step by stellar evolution only (accounting for mass loss by winds), while ΔP is the mass accreted by RLOF and by wind-mass transfer during the time-step. If necessary, the single and binary evolution step is repeated until the adaptive time-step conditions are satisfied.
For what concerns the transition from a star to a remnant, SEVN assumes that this happens at the beginning of the time-step. In this case, SEVN assigns a mass and a natal kick to the new-born compact object, based on the adopted supernova model. Then, it estimates the next time-step for the updated system.
Similarly, SEVN does not use the general adaptive time-step criterion when one of the following processes takes place: RLOF circularisation, merger, or CE. In such cases, SEVN uses an arbitrarily small time-step ($dt_{tiny} = 10^{-15}$Myr) and calculates only the aforementioned process during such time-step. Then, it estimates the new time-step.
The SEVN temporal evolution scheme is summarised in Figure 4.2 [27].

Change of interpolating tracks

During its evolution a star can change significantly its mass due to binary evolution and in particular to processes like mass loss/accretion, or stellar merger. In this case SEVN needs to find a new evolutionary track that better matches the current stellar properties.
The criteria followed by SEVN to decide if a change of track is necessary depend on the structure of stars, in particular if they have or not a decoupled core. For stars without a clear separation between core and envelope (MS H-stars or core He burning pure-He stars), SEVN moves onto a new evolutionary track every time the net cumulative mass variations due to binary processes (RLOF, wind mass accretion) is larger than 1% of the current star mass. If a star has a decoupled core (He or CO), its properties are what drive the evolution of the star. For this reason, unless there is a change in core mass, no change of track is admitted.
When a star moves to a new track, SEVN searches the track that best matches the mass (or the mass of the core) of the current star at the same evolutionary stage (SEVN phase and percentage

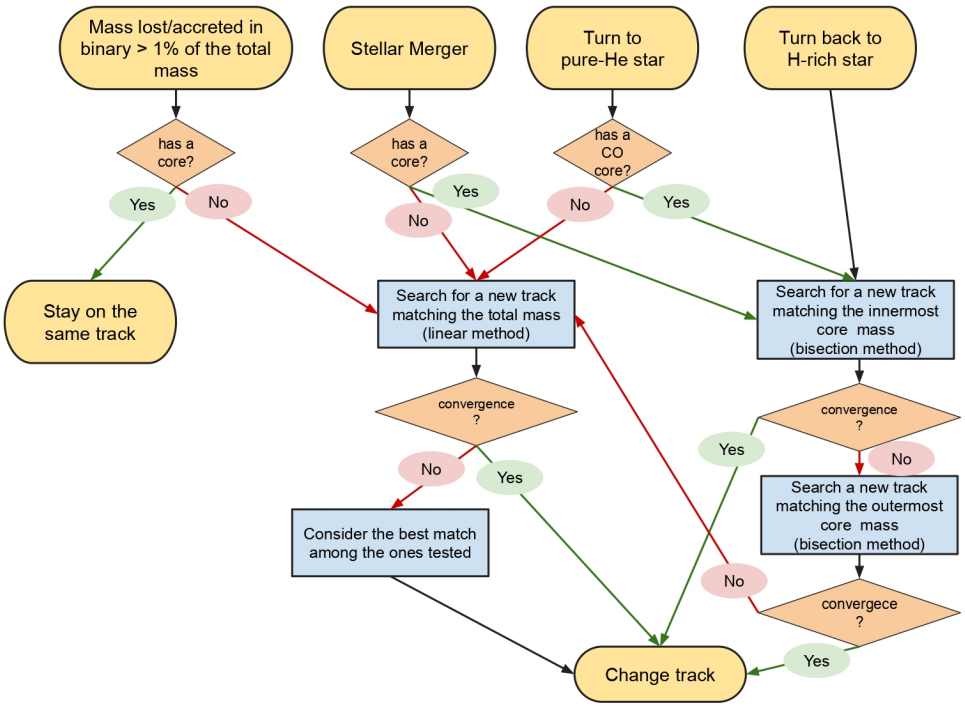

Figure 4.3: Schematic representation of the algorithm SEVN uses during a change of stellar track. The elements in the upper row indicate all the cases for which the code searches for a new stellar track: a significant mass loss/mass accretion due to binary interactions, a stellar merger, an H-rich star that loses its envelope turning into a pure-He star, and a pure-He star that accretes a new H envelope turning back into a H-rich star. In stars with both an He and CO cores, the latter is the innermost core. In stars with only an He core the innermost and outermost cores coincide.

of life) and metallicity. We define the ZAMS mass of this new track as $M_{ZAMS,new}$. In general, SEVN searches the new track in H table for H-rich stars or in pure-He table for pure-Helium stars. The only exceptions occur when a H-rich star is turned into a pure-He star (in this case SEVN jumps to pure-He tables) or when a pure-He is transformed in a H-rich (SEVN jumps from a pure-He table to a H-rich one).

SEVN adopt two different strategies to find $M_{ZAMS,new}$ for stars with or without a core. For stars without a core-envelope separation, SEVN finds the best $M_{ZAMS,new}$ following the method implemented in Spera et al. (2019, [36], see their Appendix A2). Hereafter, M is the current mass of the star, M_p is the mass of the star with ZAMS mass M_{ZAMS}, estimated at the same phase and percentage of life of the star that is changing track. $M_{ZAMS,old}$ is the ZAMS mass of the current interpolating track. Assuming a local linear relation between M_{ZAMS} and M_p, we

can estimate $M_{ZAMS,new}$ using the following equation:

$$M = \frac{M_{p,2} - M_{p,1}}{M_{ZAMS,2} - M_{ZAMS,1}} (M_{ZAMS,new} - M_{ZAMS,1}) + M_{p,1}. \tag{4.10}$$

As a first guess we set $M_{ZAMS,1} = M_{ZAMS,old}$ and $M_{ZAMS,2} = M_{ZAMS,old} + 1.2\delta M$, where δM is the cumulative amount of mass loss/accreted due to binary processes. $M_{ZAMS,new}$ is accepted as the new ZAMS mass if the following condition is fulfilled:

$$\frac{|M_{p,new} - M|}{M} < 0.005. \tag{4.11}$$

If it is not satisfied, Eq. 4.10 is iterated replacing $M_{ZAMS,2}$ or $M_{ZAMS,1}$ with the last estimated $M_{ZAMS,new}$. The iteration stops when the condition 4.11 is satisfied, or after 10 steps, or if $M_{ZAMS,new}$ is outside the range of the ZAMS mass covered by the stellar tables. If the convergence is not reached, the best $M_{ZAMS,new}$ will be the one that gives the minimum value of $|M_{p,new} - M|/M$ (it could also be the original $M_{ZAMS,old}$).

For stars with a core, SEVN looks for the best $M_{ZAMS,new}$ matching the mass of the innermost core M_c (He-core for stellar phases 2, 3, 4 and CO-core for phases 5, 6). For this purpose, we make use of the bisection method in the ZAMS mass range [max(M_c,$M_{ZAMS,min}$), $M_{ZAMS,max}$], where $M_{ZAMS,min}$ and $M_{ZAMS,max}$ represent the boundaries of the ZAMS mass range covered by the stellar tables. SEVN iterates the bisection method until condtion 4.11 is fulfilled considering the core masses. If the convergence is not reached within 10 steps, SEVN halts the iteration and the best $M_{ZAMS,new}$ is the one that gives the best match to the core mass.

Finally, the star jumps to the new interpolating track with ZAMS mass $M_{ZAMS,new}$. SEVN updates the four interpolating tracks and synchronises all the stellar properties with the values of the new interpolating track. The only exceptions are the mass properties (mass, He-core mass, CO-core mass). If the track-finding methods do not converge, the change of track might introduce discontinuities in these properties. To avoid this problem, SEVN evolves the stellar mass and mass of the core using

$$M_{t_1} = M_{t_0}(1 + \delta m) \tag{4.12}$$

where $\delta m = (m_{t_1} - m_{t_0})/m_{t_0}$. Here M_{t_1} and M_{t_0} are the masses of the stars, or of the cores, estimated at time t_1 and t_0, while m_{t_1} and m_{t_0} are the masses obtained from the interpolating

tracks at time t_1 and t_0 (see 4.2.1). Figure 4.3 summarises the algorithm SEVN uses to check and handle a change of track [27].

5

Evolution across cosmic time

In Chapter 4 we have seen how to obtain catalogs of binary and single stellar populations, by means of population synthesis codes like SEVN. From them, through proper data analysis, we can obtain a variety of information on systems of our interest, in our case on PISNe and PPISNe.
Thanks to this data we are also able to reconstruct and model the cosmic evolution of this kind of systems, reaching one of the goals of our work. In particular we can find out the cosmic evolution of PISN and PPISN rate density, learning how much of these events were produced during the Universe history. With such information we can understand how much pair-creation instability processes were common at high redshift (z) for stars formed in cosmological epoch.
The approach we used to obtain the PISN and PPISN event rate density consists in interfacing the catalogs, obtained from population synthesis, with data-driven prescriptions for the cosmic evolution of star formation rate (SFR) and metallicity. For this reason we dedicate part of this chapter to the description of these concepts, before describing the code implementation to obtain the event rates.

5.1 Cosmic star formation rate

Deriving the history of star formation in galaxies essentially involves inferring mass from light. We observe the emission from galaxies at various wavelengths, and from those measurements, we try to infer the rates at which galaxies are forming stars. Virtually all observational tracers of

star formation measure the rate of massive star formation, because massive stars emit most of the energy from a young stellar population. However, different observational tracers are sensitive to different ranges of stellar masses; hence, they respond differently as a function of stellar population age. For example, Hα emission arises primarily from HII regions photoionized by O-type stars with lifetimes shorter than 20 Myr, whereas the UV continuum is produced by stars with a broader mass range and with longer lifetimes. Newly formed stellar populations emit radiation over a broad spectrum.
In general the wavelength regimes most used to perform conversion from luminosity to SFR, and then SFR density (SFRD), are the UV and IR. Thanks to data provided by surveys at these wavelengths, we obtain best-fit luminosity function parameters and with them compute the luminosity density at the above-mentioned wavelengths. Multiplying the luminosity density by properly defined conversion factor we can finally obtain measurements of the "observed" SFRD. We now show, more in detail, how from observations in UV and IR regimes we can obtain a functional form for the star formation rate density $\psi(z)$ following the review from Madau & Dickinson (2014, [43]).

UV light

For an IMF like Salpeter's one, low-mass stars dominate the mass integrated over the whole stellar population, but at young ages, the luminosity is dominated by UV emission from massive stars. These stars have short lifetimes, so the UV emission fades quickly. Bolometrically, at least half of the luminous energy that a simple stellar population produces over a 10 Gyr cosmic lifetime emerges in the first 100 Myr, mostly in the UV, making this a natural wavelength from which to infer SFRs.
For a galaxy forming stars at a constant rate, the 1500-$\mathring{A}$ luminosity stabilizes once O stars start to evolve off the main sequence. For solar metallicity, by an age of $10^{7.5}$ years, the 1500-$\mathring{A}$ luminosity has reached 75% of its asymptotic value, although convergence is somewhat slower at lower metallicity. For these reasons, the far UV luminosity at wavelengths of $\sim 1500\mathring{A}$ (wavelengths from $1400\mathring{A}$ to $1700\mathring{A}$ have been used in the literature for both local and high redshift studies) is regarded as a good tracer of the formation rate of massive stars.
Far what concerns the measurements at these wavelengths, it is accessible with ground-based facilities for redshifts $z \gtrsim 1.4$, while measurements at lower redshifts require space-based UV data or are limited to longer UV wavelengths. In literature also mid-UV wavelengths (2300 and 2800 $\mathring{A}$) have been used. The mid-UV emission from a galaxy can have a larger contribution from longer-lived, lower-mass stars, particularly at later ages, and the time evolution of the lumi-

nosity is more gradual. This contribution become more and more important after ~ 250 Myr, when the 1500-$\mathring{A}$ of simple stellar populations drops of sharply, while the 2800-$\mathring{A}$ luminosity fades at an approximately exponential rate. This complicates the conversion from luminosity to SFR as well as any correction for dust extinction. Still, for young ages, both shorter and longer UV wavelengths usefully trace the SFR and have been used extensively in the literature. The UV luminosity output by a stellar population also depends on its metallicity. Generally speaking, less-metal-rich stars produce more UV light. The amplitude of this effect is not insignificant and depends on the details of the star formation history (SFH). Because of this dependence we expect significant evolution of the conversion factor, between luminosity and SFR, as the global metallicity of galaxies evolves.
We express the conversion factor between the intrinsic FUV (far UV) specific luminosity L_ν and the SFR as

$$SFR = K_{FUV} \times L_\nu(FUV), \tag{5.1}$$

where $L_\nu(FUV)$ is in units of $erg\, s^{-1} Hz^{-1}$ and SFR in units of $M_\odot\, yr^{-1}$. The precise value of the conversion factor K_{FUV} is sensitive to the recent SFH and metal-enrichment history as well as to the choice of IMF.
The greatest inconvenience for UV measurements of star formation is the obscuring effect of dust. Extinction is strong in the UV, so even modest amounts of dust can dramatically suppress the emerging UV flux. Dust re-emits the absorbed energy in the IR, so a reliable measurement of SFRs from UV light must either correct for the effects of dust absorption or measure the absorbed energy directly through IR emission.

IR light

The energy that dust absorbs from the UV is re-radiated at mid-IR (MIR) and far-IR (FIR) wavelengths, making IR observations another important tool for measuring SFRs. The total IR luminosity (L_{IR}, usually defined as being integrated over the wavelength range $8-1000\,\mu m$) is a measurement of the energy that was absorbed by dust mainly at UV wavelengths. Since most UV emission comes from star formation, the IR luminosity is often interpreted as being directly proportional to the absorbed fraction of the energy from star formation. However there are some processes in galaxies that can bring to IR emission in a non star-forming environment. For example active galactic nuclei (AGNs) can also produce strong UV emission, often in dusty environments, and may contribute to IR emission by heating dust in the clouds surrounding the AGN. Moreover older stellar populations can heat dust in the interstellar medium con-

tributing to FIR emission. This effect is mostly relevant for mature galaxies with low current SFR. However, for very actively star-forming galaxies without AGN, it is generally assumed that most of the IR emission arises from new star formation.
Arising from various components heated to different temperatures, the spectrum of dust emission is fairly complex and variation in dust emission from galaxy to galaxy can lead to significant uncertainties in the estimation of SFRs.
MIR and FIR observations require space-based telescopes, but at submillimeter and millimeter wavelengths, observations can be made from the ground within certain atmospheric transmission windows. In analogy with 5.1, we express the conversion from IR luminosity (L_{IR}) to ongoing SFR as

$$SFR_{IR} = K_{IR} \times L_{IR} \tag{5.2}$$

where L_{IR} is the IR luminosity integrated over the wavelength range from 8 to $1000\,\mu m$. Here, it is assumed that the IR emission is entirely due to recent star formation, but in practice, AGN and older stars can contribute to dust heating. Furthermore, if the net dust opacity to young star-forming regions in a galaxy is not large and if a significant amount of UV radiation emerges, then the SFR derived from the IR luminosity will represent only a fraction of the total. Hence, we write SFR IR in Eq. 5.2 to indicate that this is only the dust-obscured component of the SFR. Since the dust luminosity is primarily reprocessed UV emission from young star formation, the conversion factor K_{IR} also depends on the details of the SFH and on metallicity.
For what before-mentioned we sum the SFRs derived from the observed IR and UV luminosity densities, the latter uncorrected for extinction obtaining

$$SFR_{tot} = K_{FUV} L_{FUV} + K_{IR} L_{IR} \tag{5.3}$$

where L_{FUV} in the observed FUV luminosity at $1500\mathring{A}$ with no correction for extinction and the definition of K_{FUV} here is, of course, different from the one in Eq. 5.1 since here the UV luminosity is not per unit frequency ($L_{FUV} = \nu L_{\nu}$).
So the best way to account for the effect of dust attenuation is to directly measure the energy emitted at both UV and IR wavelengths, i.e., both the luminosity that escapes the galaxy directly and that which is absorbed and reradiated by dust.

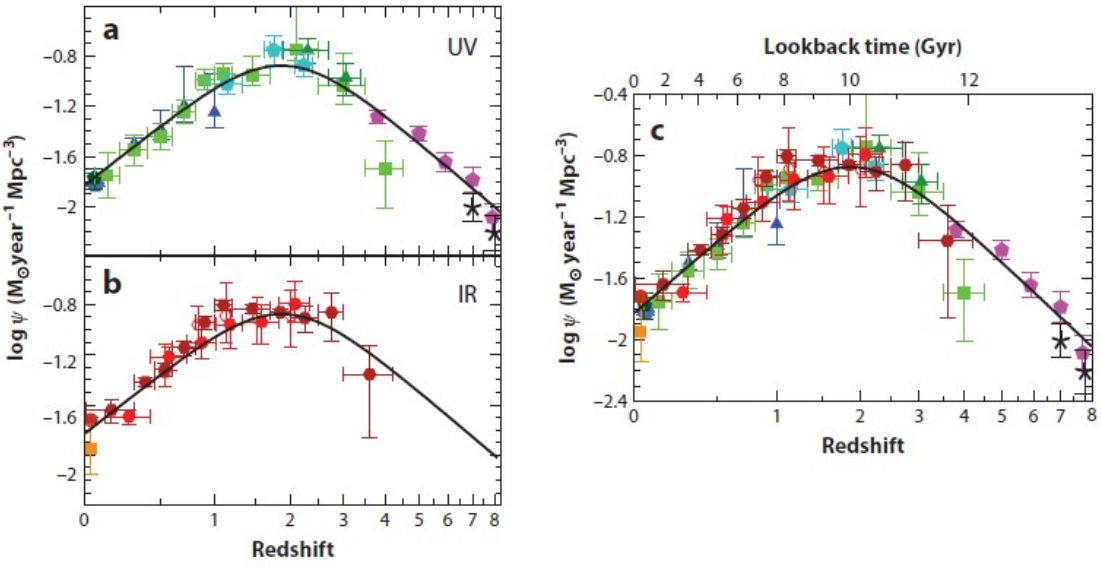

Figure 5.1: The history of cosmic star formation from (a) FUV, (b) IR, and (c) FUV+IR measurements. The solid curve in the three panels plots the best-fit SFR density in Eq. 5.5. Taken from Madau & Dickinson (2014, [43]).

Star formation rate density

As briefly illustrated at the beginning of the chapter, Madau et al. (1996, 1998 [44][45]) and Lilly et al. (1996, [46]) developed a method where data from galaxy surveys were used to infer the SFRD $\psi(t)$ directly.

The only surveys included in the review by Madau & Dickinson (2014, [43]) are those that measured SFRs from FUV or MIR and FIR measurements. All the surveys used here provide best-fit luminosity function parameters – generally Schechter functions for the UV data, but other functions for the IR measurements. These allowed them to integrate the luminosity function down to the relative limiting luminosity in units of the characteristic luminosity L_*. Adopting an integration limit $L_{min} = 0.03L_*$ when computing the luminosity densities, is possible to find, for the Schechter function

$$\rho_{FUV}(z) = \int_{0.03L_*}^{\infty} L\phi(L,z)dL = \Gamma(2+\alpha, 0.03)\phi^* L_*. \tag{5.4}$$

Here α denotes the slope of the Schechter parametrization, Γ is the incomplete gamma function and ϕ^* is the normalization of the Schechter luminosity function. Multiplying the integrated FUV and IR comoving luminosity densities by the conversion factors K_{FUV} and

K_{IR}, we obtain measurements of the "observed" UV and IR SFRDs. Madau & Dickinson (2014, [43]) estimated the conversions factors to be $K_{FUV} = 2.5 \times 10^{-10} \mathrm{M}_{\odot}\, yr^{-1} L_{\odot}^{-1}$ and $K_{IR} = 1.73 \times 10^{-10} \mathrm{M}_{\odot}\, yr^{-1} L_{\odot}^{-1}$ valid for a Salpeter IMF.
From these prescriptions we can finally find the best-fitting function for SFRD

$$\psi(z) = 0.015 \, \frac{(1+z)^{2.7}}{1 + [(1+z)/2.9]^{5.6}} \mathrm{M}_{\odot}\, yr^{-1} Mpc^{-3} \tag{5.5}$$

that can also be visualized in Figure 5.1.

5.2 Metallicity evolution

Understanding the metallicity evolution through cosmic time is essential when tracing the evolution of whatever process in cosmological epochs. For this reason, in order to learn how the PISN and PPISN event rate varies with redshift, we first need to understand how metallicity varies with redshift.
To reach this goal is necessary to know the chemical properties for high-redshift galaxies. Thinking to extract these properties directly from the faint starlight emitted by star-forming galaxies at high redshift is extremely difficult. For this reason is better to focus for example on protogalactic gas detected in absorption against bright background quasars.
The high-redshift Universe is occupied by populations of objects spanning a wide range of metallicities going from [Z/H] ≈ 0 (e.g. quasars) to [Z/H] = 3 like diffuse large-scale configurations such as the Ly-α forest clouds. Systems with a mean metal abundance that lie between these two extremes are the damped Ly-α absorption systems (DLAs). A lot of studies used these systems to reconstruct the metallicity history of the Universe, e.g. Prochaska et al.(2003, [47]); Kulkarni et al. (2007, [48]); Rafelski et al. (2012, [49]); De Cia et al. (2018, [50]).
The DLAs are very useful for several reasons. First, since they are detected in absorption, they are unbiassed with respect to luminosity and presumably mass. Second, in contrast to all other classes of quasar absorption systems, the gas in DLAs is mainly neutral. In fact, DLAs dominate the neutral-gas content of the Universe out to $z \sim 5$ and exhibit properties indicating that they are neutral-gas reservoirs for star formation at high redshift. Moreover, the large optical depth at the Lyman limit of the neutral gas in DLAs (typically $\tau_{LL} \approx 10^4$) eliminates the need for uncertain ionization corrections to deduce the metal abundances [49]. In other words since DLAs trace gas-rich galaxies out to high redshift, and regardless of their luminosity, they

provide an attractive way of measuring the evolution of the metallicity of the neutral gas with cosmic time.
In order to get a more precise estimate of the evolution of metallicity with redshift dust corrections are needed. In fact the higher the condensation temperature of a metal, the lower its abundance that we can measure in the gas-phase. It became soon evident that large fractions of the refractory metals were missing from the observed gas-phase, because they were instead locked into dust grains. This phenomenon is called dust depletion.
De Cia et al. (2018, [50]), that took into account dust depletion in their work, applied the dust correction to as many DLA abundances as available in the literature, with sufficient relative abundances measurements to derive a sensible dust-correction and with redshift between 0 and 5. They found the behaviour of [Fe/H] with respect to z. Here they chose [Fe/H] as a reference for metallicity essentially because Fe is among the metals that are most easily measured, and therefore most widely available.
The best fit to the data is the linear fit $[\text{Fe/H}] = A + B \times z$, where $A = -0.18 \pm 0.21$ and $B = -0.24 \pm 0.14$. The quoted uncertainties on both A and B are at 1σ, assuming that the observational values follow a Gaussian distribution. From here is possible to see that the metallicities decreases with redshift and De Cia et al. (2018, [50]) did not find evidence for a steepening of the evolution of metallicity at high z, even if more measurements are needed to draw solid conclusions on the high-redshift regime.

5.3 COSMORATE

Now that we have outlined the star formation rate density and the metallicity evolution, we can describe how the knowledge of this properties allows us the obtain event rate densities for pair instability processes and, more in general, for a whatever process we are taking into exam, e.g. the merger rate density of binary compact objects.
As stated at the beginning of the chapter, this further step is feasible interfacing catalogs obtained from population synthesis, in our case from SEVN, with data-driven prescriptions for the evolution of the SFRD and metallicity. This is effectively implemented by means of the semi-analytic code COSMORATE by Santoliquido et al. (2020, [51]; 2021, [52]) that is computationally optimised to extensively probe the parameter space.

What COSMORATE does, consist essentially in evaluating the following equation

$$\mathcal{R}(z) = \frac{d}{dt_{lb}(z)} \left[\int_{z_{maz}}^{z} \psi(z') \frac{dt_{lb}(z')}{dz'} dz' \int_{Z_{min}}^{Z_{max}} \eta(Z)\, \mathcal{F}(z', z, Z)\, dZ \right]. \tag{5.6}$$

This integral gives us the variation of the event rate density of a process with the redshift, if we feed the code with catalogs regarding the process we are interested in. As above-mentioned it can be used to provide PISN, PPISN or even merger rate density evolution of binary compact objects, if we implement this catalogs. Moreover the evaluation of merger rate density is the usage for which COSMORATE was initially meant by Santoliquido et al. (2020, [51]).
In Eq. 5.6 $t_{lb}(z)$ is the look-back time at redshift z, Z_{min} and Z_{max} are the minimum and maximum metallicity we are using, $\psi(z')$ is the cosmic SFRD at redshift z', $\mathcal{F}(z', z, Z)$ is the fraction of systems undergoing PISN/PPISN that form at redshift z' from stars with metallicity Z and exploding at redshift z. $\eta(Z)$ is the PISN/PPISN efficiency, namely the ratio between the total number $\mathcal{N}_{TOT}(Z)$ of systems exploding within an Hubble time and the total initial mass $M_*(Z)$ of the simulation with metallicity Z:

$$\eta(Z) = f_{bin}\, f_{IMF}\, \frac{\mathcal{N}_{TOT}(Z)}{M_*(Z)} \tag{5.7}$$

where f_{bin} is the binary fraction, and f_{IMF} is a correction factor that takes into account account that only stars with mass higher then a certain threshold are simulated. This parameter depends on the threshold and on the IMF. For example, in a simulation of a population of stars following a Kroupa IMF with mass higher the $5\mathrm{M}_\odot$ and mass exponent $\alpha = 2.3$ we have $f_{IMF} = 2.85$.
For what concerns the SFRD, we use the one described by Madau & Fragos (2017, [53]):

$$\psi(z) = 0.01\, \frac{(1+z)^{2.7}}{1 + [(1+z)/3.2]^{6.2}} \mathrm{M}_\odot\ \mathrm{yr}^{-1}\, \mathrm{Mpc}^{-3}. \tag{5.8}$$

This is an updated version of Eq. 5.5 that better reproduces a number of recent $4 \lesssim z \lesssim 10$ results. Moreover the normalization factor has been multiplied by 0.66 to convert SFRs from a Salpeter initial mass function to a Kroupa IMF [53].
In the function $\mathcal{F}(z', z, Z)$ is involved the average metallicity evolution that we have treated in section 5.2. In COSMORATE this quantity is implemented through the fitting formula

found by De Cia et al. (2018, [50]):

$$\mu(z) = \log\left(\frac{Z(z)}{Z_\odot}\right) = \log\ a + b\,z \tag{5.9}$$

where the slope b is the same as in the previous section $b = -0.24 \pm 0.14$, while the intercept is different being $a = 1.04 \pm 0.14$. This update has been performed by Santoliquido et. al (2020, [51]) since the original fit yields a metallicity $Z(z = 0) = 0.66\ Z_\odot$, which is low compared to the average stellar metallicity measured at redshift zero. Hence, the equation has been rescaled to yield $Z(z = 0) = (1.04 \pm 0.14)\, Z_\odot$, where $Z_\odot = 0.019$, consistent with the average metallicity of galaxies at $z \sim 0$ from the Sloan Digital Sky Survey.
In COSMORATE the distribution of stellar metallicities $\log(Z/Z_\odot)$, at a given redshift, is modelled as a normal distribution with mean value $\mu(z)$, from Eq. 5.9, and standard deviation $\sigma_Z = 0.20$ dex as our fiducial value:

$$p(z', Z) = \frac{1}{\sqrt{2\pi\sigma_Z^2}} \exp\left\{-\frac{[\log(Z/Z_\odot - \mu(z')]^2}{2\sigma_Z^2}\right\}. \tag{5.10}$$

The fraction of systems undergoing PISN/PPISN that form at redshift z' from stars with metallicity Z and merge at redshift z is thus given by

$$\mathcal{F}(z', z, Z) = \frac{\mathcal{N}(z', z, Z)}{\mathcal{N}_{TOT}(Z)}\, p(z', Z) \tag{5.11}$$

where $\mathcal{N}(z', z, Z)$ is the total number of systems undergoing PISN/PPISN at redshift z and form from stars with metallicity Z at redshift z'.
$\mathcal{F}(z', z, Z)$ and $\eta(Z)$ are the functions in which enter the information from population synthesis catalogs that we use as input. The mandatory parameters of input are the total initial mass of the simulation (entering in $\eta(Z)$) and the delay times (time elapsed from the birth of the system to its explosion) of each system in the catalog. Then there are other non-mandatory quantities that is possible to include as input, e.g. the initial masses.
Another feature of COSMORATE consist in the fact that it can sample the input data to create catalogs of specific systems – e.g. systems that undergo PISNe or PPISNe – at a given redshift.

6 Simulations and results

In this chapter we present the methods used and the results obtained from the simulations we performed.
As already discussed in Chapters 4 and 5, we used SEVN to simulate the evolution of binary and single populations of stars, investigating pair-creation instability processes. Then by means of COSMORATE, we evaluated PISNe and PPISNe rate density evolution with z.
We performed simulations to explore the dependence of pair instability occurrence on different parameters, e.g. metallicity and IMF. In particular we worked with several populations of systems, each of them with different metallicity. These samples correspond to just as many SEVN initial conditions (ICs). From them we therefore obtained the catalogs to feed COSMORATE. Furthermore, we analysed data from previous SEVN runs, simulating Pop. III stars, by Costa et al. (2023, [54]).

6.1 First sample

6.1.1 SEVN simulations

The initial conditions for the SEVN sample were generated by means of the python module IC4popsyn from Giacobbo (2021, [55]). This module is specifically developed to generate initial conditions for SEVN. These consist of an input file in which each line contains the initial

Z	PISN rate SSE (%)	PPISN rate SSE (%)	PISN rate BSE (%)	PPISN rate BSE (%)
10^{-11}	0.53	3.43	0.91	3.42
10^{-6}	0.61	1.98	1.11	2.53
10^{-4}	0.57	4.32	1.11	4.83
2×10^{-4}	0.27	4.61	0.85	5.32
4×10^{-4}	0.00	4.87	0.64	5.97
5×10^{-4}	0.00	4.86	0.64	5.96
6×10^{-4}	0.00	4.85	0.57	5.81
8×10^{-4}	0.00	4.84	0.80	5.72
10^{-3}	0.09	4.73	1.06	5.16
2×10^{-3}	0.98	3.14	2.20	3.17
4×10^{-3}	0.96	3.69	2.76	3.76
5×10^{-3}	0.81	3.80	2.44	4.31
8×10^{-3}	0.09	4.09	1.40	5.79
10^{-2}	0.00	3.50	0.71	6.03
1.4×10^{-2}	0.00	1.29	0.12	3.71
1.7×10^{-2}	0.00	0.04	0.00	1.64

Table 6.1: PISN and PPISN rates per each metallicity with respect to the total number of supernovae for single and binary evolution

parameters of a unique system. For single stars the parameters are ZAMS mass, metallicity, stellar spin, supernova model, age of the star at the beginning of the simulation, age at which the simulation is stopped and the times at which the output is stored. For binary systems we have the above-mentioned parameters for both stars, in addition to initial eccentricity and semi-major axis.

With IC4popsyn input files can be created according to two possible models: one based on the calculations by Sana et al. (2012, [24]) and the other, still based on Sana et al. (2012, [24]), but with the eccentricities computed following Eq. 3 in Moe & Di Stefano (2017, [56]). Among them we used the second one.

Therefore we generated 10^6 binary systems with a primary mass between $5M_\odot$ and $150M_\odot$ following a Kroupa initial mass function. The slope of the broken power-law of the IMF was set to $\alpha = 2.3$. Moreover the secondary mass is always higher than $2.2M_\odot$, while the stellar spin and the supernova model were set respectively to zero and *delayed* – see Section 4.2.

From this ICs for binary systems we have generated 2×10^6 ICs for single stellar systems using

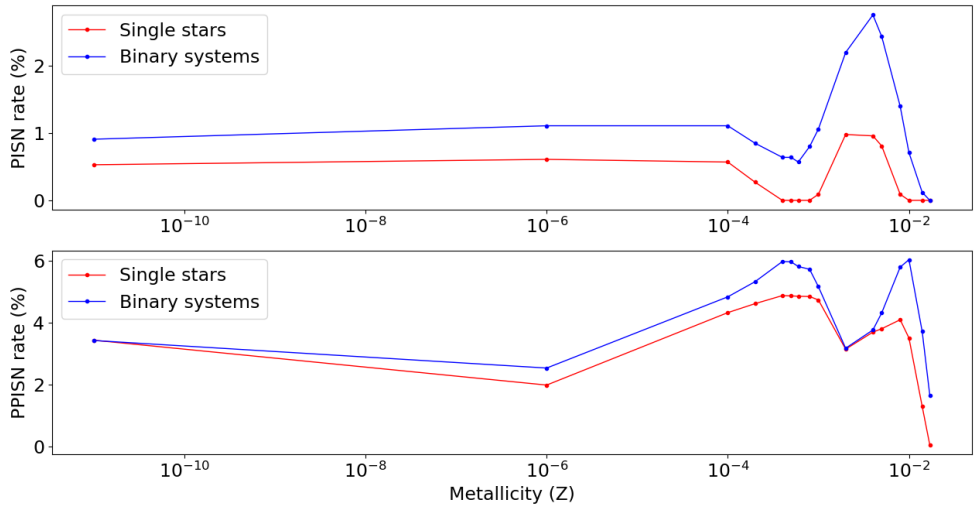

Figure 6.1: PISN and PPISN rates variation with metallicity for binary and single stellar systems. Here the metallicty axis is in logarithmic scale to highlight the behaviour at low metallicity.

the same ZAMS masses of the binaries. In this way is easier to make direct comparison between the outcomes of the two cases.

For both binaries and single stars, we explored a wide range of metallicities, going from the most metal poor case to quasi-solar metallicity ($Z = 10^{-11}, 10^{-6}, 10^{-4}, 2\times10^{-4}, 4\times10^{-4}, 5\times10^{-4}, 6\times10^{-4}, 8\times10^{-4}, 10^{-3}, 2\times10^{-3}, 4\times10^{-3}, 5\times10^{-3}, 8\times10^{-3}, 10^{-2}, 1.4\times10^{-2}, 1.7\times10^{-2}$). We set Z as a runtime option, evolving for each metallicity all the 10^6 binaries and 2×10^6 single stars. We performed the evolution for all the systems from the ZAMS to the end of stars life.

Analysing the data provided by SEVN for each metallicity, we were able to calculate the rates of occurrence of PISNe and PPISNe. These are reported in Table 6.1, where we show the rates, for binaries and single stars, with respect the total number of supernovae. Moreover the behaviour of PISN and PPISN rates with respect to metallicity are shown in Figure 6.1.

The PISN rate reaches a peak in correspondence of $Z \sim 10^{-3} - 10^{-2}$, while in the same range of metallicities PPISNe are a little depleted. Anyway PPISNe are always more frequent with respect to PISNe. This can be easily explained from the lower mass range required for PPISN events and the shape of Kroupa IMF, that favor low mass stars. In all the cases very high metallicities correspond to a strong reduction on PISN and PPISN occurrence. In fact, we expect pair instability processes to happen in very massive, metal-poor stars as already discussed in Section 2.1.

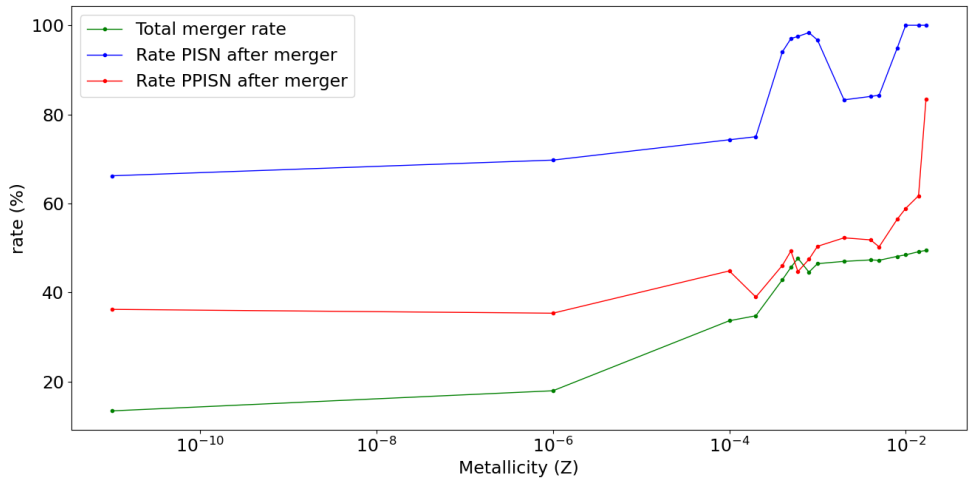

Figure 6.2: Rates of PISN and PPISN occurred after merger with respect to the total number of PISN and PPISN. We also display the total merger rate evolution with respect to metallicity.

The most important feature that we can extrapolate from the plots is that rates for binary systems are higher than single stars, at all metallicities. This is a confirmation of what discussed in Chapter 3 about the strong influence of binary processes on stellar evolutionary path. In particular in our work we focused on stellar merger events. Therefore among all the evolved binary systems we selected those undergoing pair-creation instability after a merger event. The rates of PISN/PPISN occurred after a merger with respect to the total number of PISN/PPISN, at each metallicity, are shown in Figure 6.2. Here is also reported the total merger rate with respect the total number of binaries.

From Figure 6.2 is clear that mergers have an essential role for PPISNe and – even more – for PISNe, in particular at highest metallicities. Indeed, at these metallicities 100% – or nearly – of PISNe occur after a merger. This can be explained from the fact that stars produced by a merger are highly more massive than the two progenitor stars singularly. Therefore it is more likely that this star is in the PISNe or PPISNe mass range. Furthermore, looking at the total merger rate in the plot, we see that, on average, it increases with Z, reaching also peaks of about 50%. This might suggest that also the intrinsic increase of merger events, at high Z, could be a cause of the higher rate of pair-creation instability after mergers.

On the other hand, at lower metallicities mergers seem to be less relevant. In Figure 6.3 are represented the rates of PISNe and PPSINe in binaries where no previous merger event occurred. In this way we disentangle the rates from the dependence on mergers. Here we can notice that the amount of supernovae occurring without a previous merger are higher at lower

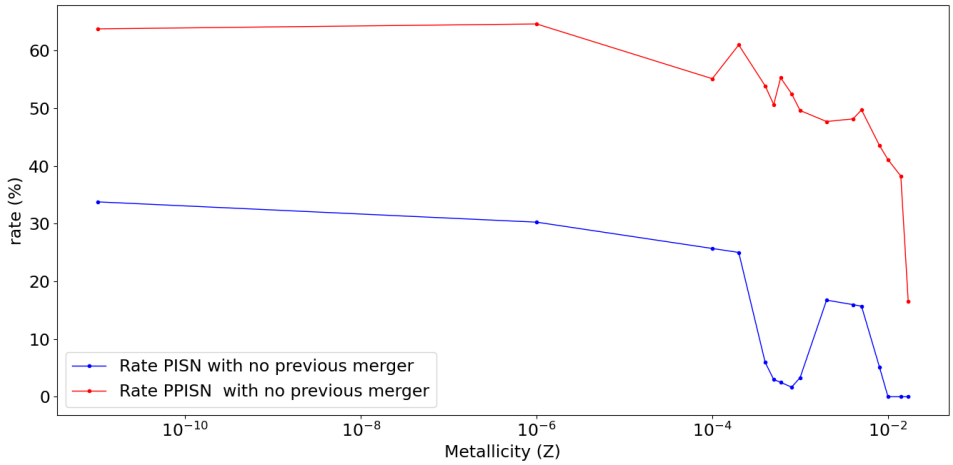

Figure 6.3: Rates of PISNe and PPISNe in binary systems that have not experienced a merger before the supernova.

metallicity. This again reinforces the idea that metal-poor environments favor pair-instability processes. Indeed, as discussed in Chapter 2, at high metallicity stellar winds are more efficient. Therefore, in this context, stellar mergers are essential to form very massive stars that are the progenitors of PISNe and PPISNe. In other words, at very low metallicity more stars can produce a pair-creation instability without the need of merging with their companions. At very high metallicity instead, binary mergers seems to be an unavoidable condition to have PPISN and even more PISN.

6.1.2 COSMORATE RUNS

Based on the data analysis of SEVN output, we produced ICs suitable for COSMORATE – see Chapter 5. Therefore we created input files considering the total amount of PISNe/PPISNe found. In addition to this, we split-up ICs for binaries, creating input files collecting specific events, e.g. PISNe/PPISNe occurring after or before a merger. In this way we were able, not only to analyse the evolution with z of the rate density of the total number of supernovae, but also of more specific events involving a merger in the system.

The input files, as already mentioned in Chapter 5, contain the total stellar mass simulated and the delay time of each system as mandatory parameter. Then there are other non-mandatory parameters that, in our case, depend on the events we are considering. In particular for the case of supernovae occurring after a merger, we added the ZAMS mass of the two components of the binary, the mass of the star born from the merger and the pre-supernova mass. Instead, if

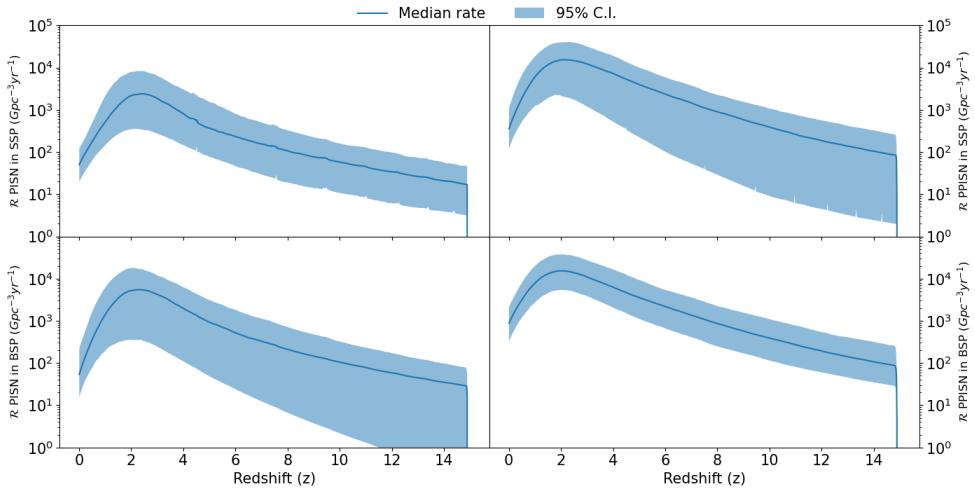

Figure 6.4: Event rate density evolution with redshift for all the PISNe and PPISNe, for single and binary stellar populations reported as SSP and BSP respectively. The solid line is the median value of the distribution of rate density produced by observational uncertainties on SFRD and metallicity evolution. The blue area represents the 95% credible interval of the rate density distribution.

there were no merger involved, i.e. for single stellar systems or if the supernova occurs before a merger, we only added the ZAMS mass and the pre-supernova mass of the star. These parameters, as we are going to see, are used by the code to produce catalogs of PISNe and PPISNe at selected redshifts.

We ran COSMORATE for each set of ICs above-mentioned following Eq. 5.6 for the calculation of the event rate density. Moreover all the quantities here involved are those described in Section 5.3. In particular we performed 10^3 realisation of Eq. 5.6 per each IC. In each realisation, we randomly drew the normalisation value of the SFRD (Eq. 5.5), and the intercept and the slope of the average metallicity (Eq. 5.9) from three Gaussian distributions with mean (standard deviation) equal to $\log \psi(0) = -2$ ($\sigma_{\log \psi} = 0.2$), $a = 1.04$ ($\sigma_a = 0.14$) and $b = -0.24$ ($\sigma_b = 0.14$) respectively. For simplicity, the value of the intercept and that of the slope are drawn separately, assuming no correlation.

Figure 6.4 shows the result of the calculation of the event rate density ($\mathcal{R}$) considering all the PISNe and PPISNe found. Here we can see how the uncertainties on SFRD and metallicity evolution strongly impact on the uncertainties of the event rate density. In fact the 95% credible interval (C.I.), covers several orders of magnitude.

From Figure 6.4 we notice that the maximum of rate density is reached around $z \sim 2$. This can be easily understood looking at the SFRD plot in Figure 5.1. Star formation in fact reached a maximum around $z = 2$ and for this reason the majority of PISNe/PPISNe events prob-

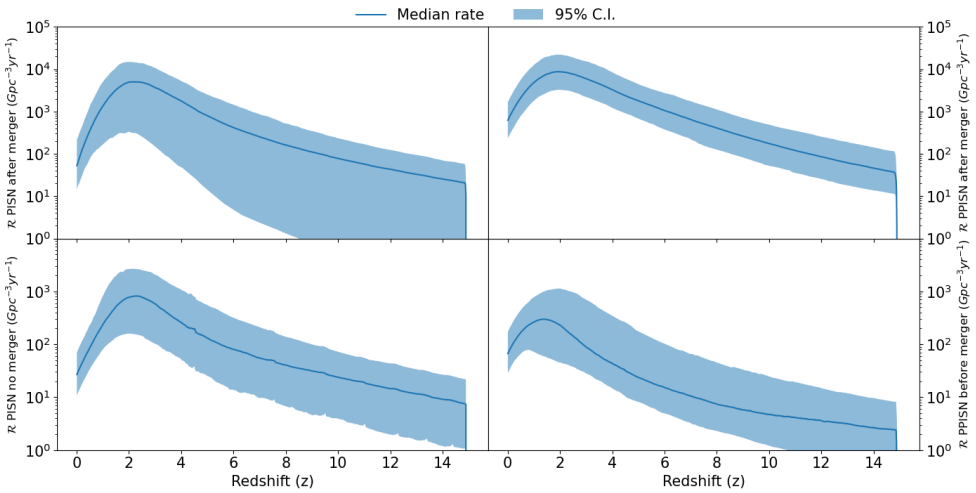

Figure 6.5: Rate density evolution of PISNe and PPISNe occurred after a binary merger and, before a merger for PPISNe and with no merger for PISNe. The solid line is the median value of the distribution of rate density produced by observational uncertainties on SFRD and metallicity evolution. The blue area represents the 95% confident interval of the rate density distribution.

ably occurred in this epoch. The rate density then decreases both at higher and lower redshift. In particular at $z \sim 0$ – present time – the PISN rate density reaches the value of $\mathcal{R} \sim 10^2\, Gpc^{-3}yr^{-1}$, while for PPISNe is around an order of magnitude higher. The decrease toward higher z is instead substantially slower than at lower redshift.

For completeness we also show in Figure 6.5 the density rates of PISNe and PPISNe occurred after a binary merger and, before a merger for PPISNe and with no merger for PISNe. We make this distinction between PPISNe and PISNe since the latter lead to the disruption of the star and no merger is anymore possible.

From the plots we see that rate densities for events not involving a previous merger are much lower with respect their counterpart. This trend hold at every redshift and is expected from what above-mentioned about mergers impact on pair instability events.

COSMORATE CATALOGS

For all the performed COSMORATE runs, we created catalogs containing the characteristics of stellar populations undergoing PISNe or PPISNe at a certain redshift. For instance in Figure 6.6 are shown the ZAMS masses of stars in SSP exploding as PISNe or PPISNe at six different redshifts ($z = 0.1, 1.0, 2.0, 4.0, 6.0, 10.0$). At higher redshift the mass distributions for

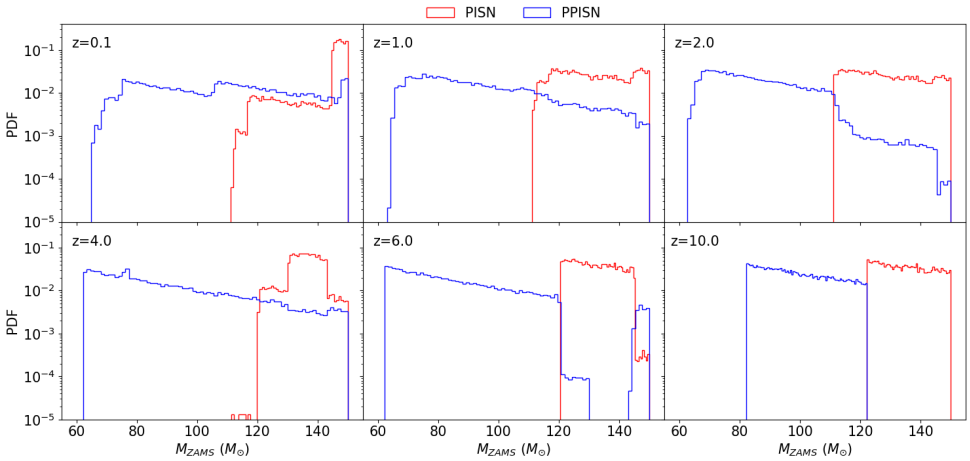

Figure 6.6: Initial mass distribution of single stars that undergo PISNe or PPISNe at $z = 0.1,\ 1.0,\ 2.0,\ 4.0,\ 6.0,\ 10.0$.

PISNe and PPISNe are sharply separated: for $M_{ZAMS} \gtrsim 120\mathrm{M}_\odot$ we have quite exclusively PISNe, while for $60\mathrm{M}_\odot \lesssim M_{ZAMS} \lesssim 120\mathrm{M}_\odot$ only PPISNe can occur. At lower redshift instead, we have PPISNe occurrence also at higher masses even if PISNe remain the most probable channel.

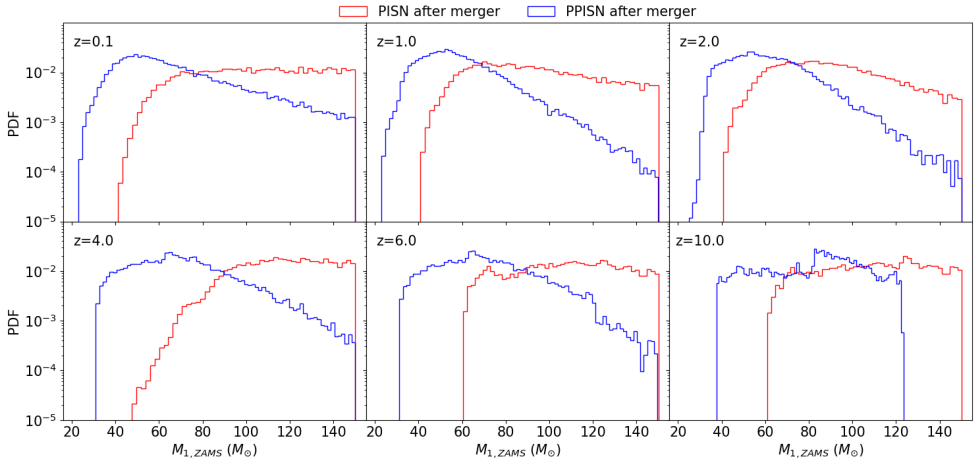

Figure 6.7: Initial mass distribution of primary stars in binary systems that undergo PISNe or PPISNe after a stellar merger at $z = 0.1,\ 1.0,\ 2.0,\ 4.0,\ 6.0,\ 10.0$.

Binary evolution can change a lot the picture with respect to single stellar evolution. In Figure 6.7 we show the distributions of ZAMS mass of the primary star in binary systems where PISNe or PPISNe occurred after a merger. The masses here are more widely distributed with respect to the previous case, reaching values even lower than $40\mathrm{M}_\odot$. Such low masses would

not be sufficient for a single star to explode as PISN or PPISN. This shows that, even if two companions of a binary system are not sufficiently massive to undergo PISN/PPISN singularly, a merger could allow the formation of a new star able to experience pair-creation instability because of its large mass. Indeed stellar mergers can create very massive stars. This is clearly shown in Figure 6.8. Here we report the distributions of masses of newly born stars immediately after merger, but selecting only the cases where these stars then undergo PISNe or PPISNe.

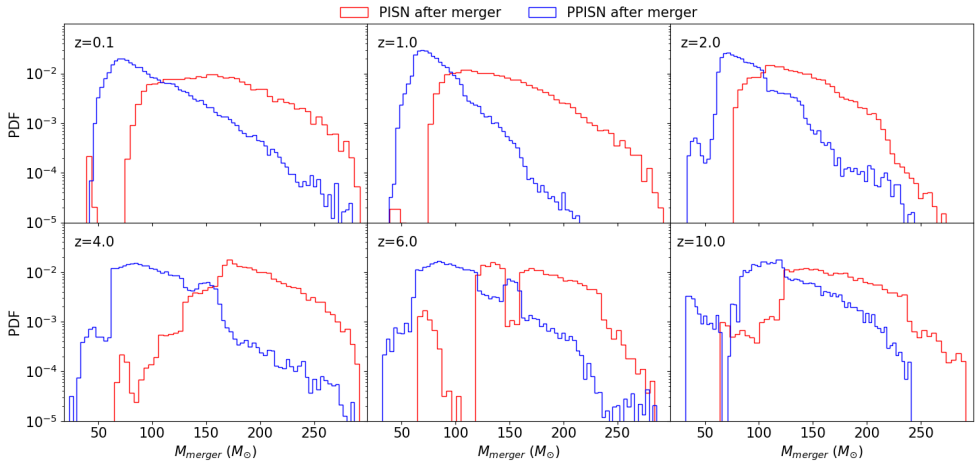

Figure 6.8: Initial mass distribution of stars formed after a binary merger at $z = 0.1, 1.0, 2.0, 4.0, 6.0, 10.0$. These distributions were found selecting exclusively systems in which a PISN or PPISN occurs after the merger.

From the plots we notice that the upper limit mass, in both the cases of PISNe and PPISNe, extends beyond the $200M_\odot$, especially at higher redshift. This of course contributes in the formation of an helium core sufficiently massive to undergo pair instability.

6.2 Population III stars

Population III stars, born from the primordial gas in the Universe, lose a negligible fraction of their mass via stellar winds and possibly follow a top-heavy mass function. Hence, they have often been regarded as the ideal progenitors of PISNe and PPISNe. For these reasons we studied the occurrences of pair instability events for this kind of stars.
Therefore we analysed the output data from the SEVN runs by Costa et al. (2023, [54]). For this work they assumed a metallicity for Pop. III stars of $Z = 10^{-11}$ and implemented all their characteristic features in the SEVN code. Indeed Pop. III stars have a very typical behaviour. For instance during the early MS, Pop. III stars cannot ignite the CNO cycle because of the

initial lack of carbon, nitrogen and oxygen. Pop. III stars need very high central temperatures to reach pressure support just with the energy provided by the proton-proton (pp) chain. Depending on the stellar mass, the central temperature becomes so high that some carbon could be synthesized from the triple-α reaction (i.e., helium burning), even in the MS. This leads the CNO cycle to ignite and suddenly replace the pp chain as the main source of energy of the star [57][58]. Moreover, due to the high central temperatures reached at the end of the MS, Pop. III stars have a smoother transition to the core helium burning phase with respect to more metal-rich stars.
Costa et al. (2023, [54]) simulated Pop. III binary systems evolving them until advanced evolutionary phases. The ZAMS mass, M_{ZAMS}, ranges from 2 to 600$M_\odot$.

6.2.1 Binary initial conditions

We now describe the SEVN initial conditions used by Costa et al. (2023, [54]) for computing binary-population catalogs.

Initial mass function

There is still no consensus about the IMF of Pop. III stars, although it should be rather top-heavy with respect to that of local stars. The sets of possible IMFs adopted are the following.

- A flat-in-log distribution:
$$\xi(M_{ZAMS}) \propto M_{ZAMS}^{-1}. \tag{6.1}$$

- A Kroupa (2001, [59]) IMF (hereafter, K01):
$$\xi(M_{ZAMS}) \propto M_{ZAMS}^{-2.3}. \tag{6.2}$$
With respect to the original K01, which has a flatter slope for $M_{ZAMS} < 0.5M_\odot$, here is assumed a single slope because are not generated ZAMS masses $< 5M_\odot$ from this distribution.

- A Larson (1998, [60]) distribution (hereafter, L98):
$$\xi(M_{ZAMS}) \propto M_{ZAMS}^{-2.35} e^{-M_{cut1}/M_{ZAMS}}, \tag{6.3}$$
where $M_{cut1} = 20M_\odot$.

- A top-heavy distribution:

$$\xi(M_{ZAMS}) \propto M_{ZAMS}^{-0.17} e^{-M_{cut2}^2/M_{ZAMS}^2}, \tag{6.4}$$

  where $M_{cut2} = 20\mathrm{M}_\odot$

- The distribution derived by Park et al. (2023, [61]), hereafter P23, based on hydrodynamical simulations of Pop. III star formation.

$$\xi(M_{ZAMS}) \propto M_{ZAMS}^{0.62} e^{-M_{ZAMS}^2/M_{cut3}^2}, \tag{6.5}$$

  where $M_{cut3} = 188\mathrm{M}_\odot$.

Mass ratio and secondary mass

The ZAMS mass of the secondary star ($M_{ZAMS,2}$) is drawn according to three different distributions.

- The distribution of the mass ratio q from Sana et al. (2012, [24]), hereafter S12:

$$\xi(q) \propto q^{-0.1}, \tag{6.6}$$

  with $q \in [0.1,\ 1]$ and $M_{ZAMS,2} \geq 2.2\mathrm{M}_\odot$.

- In the sorted distribution, the ZAMS mass of the entire star population is drawn from the same IMF, and then two stars from this distribution are randomly paired, imposing that $M_{ZAMS,2} \leq M_{ZAMS,1}$. In this model, the minimum mass of the secondary is equal to that of the primary ($5\mathrm{M}_\odot$) by construction.

- The mass ratio distribution by Stacy & Bromm (2013, [62]), hereafter SB13:

$$\xi(q) \propto q^{-0.55}, \tag{6.7}$$

  with $q \in [0.1,\ 1]$ and $M_{ZAMS,2} \geq 2.2\mathrm{M}_\odot$. This distribution was obtained from a fit to Pop. III stars formed in cosmological simulations.

The final mass ratio distribution also depends on the mass distribution of the primary star.

Orbital period

Two different distributions are used for the initial orbital period (P).

- The distribution derived by S12 for O and B type stars in the local Universe:

$$\xi(\Pi) \propto \Pi^{-0.55} \tag{6.8}$$

  with $\Pi = \log(P/day) \in [0.15,\ 5.5]$.

- The period distribution found by SB13:

$$\xi(\Pi) \propto \exp\left[-\left(\Pi - \mu\right)^2 / \left(2\sigma^2\right)\right]. \tag{6.9}$$

  This is a Gaussian distribution with $\mu = 5.5$, and $\sigma = 0.85$, favouring long periods with respect to the S12 distribution.

Eccentricity

Also orbital eccentricity is drawn according to two distributions.

- The distribution obtained by S12:

$$\xi(e) \propto e^{-0.42} \tag{6.10}$$

  with $e \in [0,\ 1)$.

- The thermal distribution, adopted for Pop. III binaries by e.g. Kinugawa et al. (2014, [63]); Hartwig et al. (2016, [64]); Tanikawa et al. (2021, [65]):

$$\xi(e) \propto e \tag{6.11}$$

  with $e \in [0, 1)$. This eccentricity distribution favours highly eccentric systems, at variance with Eq. 6.10. Recent hydro-dynamical simulations (Park et al., 2023, [61]) suggest that Pop. III binary stars form preferentially with high orbital eccentricity, favouring the distribution in Eq. 6.11 with respect to Eq. 6.10.

Model	$M_{ZAMS,1}$	M_{ZAMS}	Mass ratio q	Period P	Eccentricity e	N $[\times 10^7]$	Total mass $[\times 10^9\,\mathrm{M}_\odot]$
LOG1	Flat in log	–	S12	S12	S12	1.45	2.59
LOG2	Flat in log	–	S12	SB13	Thermal	1.45	2.58
LOG3	–	Flat in log	Sorted	S12	S12	1.38	3.19
LOG4	Flat in log	–	SB13	S12	Thermal	1.53	2.60
LOG5	Flat in log	–	SB13	SB13	Thermal	1.53	2.60
KRO1	K01	–	S12	S12	S12	5.23 (2.00†)	1.35 (0.89†)
KRO5	K01	–	SB13	SB13	Thermal	6.11 (2.00†)	1.52 (0.93†)
LAR1	L98	–	S12	S12	S12	2.00	1.20
LAR5	L98	–	SB13	SB13	Thermal	2.27 (2.00†)	1.30 (1.24†)
TOP1	Top heavy	–	S12	S12	S12	1.05	4.16
TOP5	Top heavy	–	SB13	SB13	Thermal	1.07	4.03
PAR1	P23	–	S12	S12	S12	1.05	2.35
PAR5	P23	–	SB13	SB13	Thermal	1.06	2.28

Table 6.2: Column 1 reports the model name. Columns 2 describes how we generate the ZAMS mass of the primary star (i.e., the most massive of the two members of the binary system). Column 3 describes how we generate the ZAMS mass of the overall stellar population (without differentiating between primary and secondary stars). We follow this procedure only for model LOG3. Columns 4, 5 and 6 specify the distributions we used to generate the mass ratios, the orbital periods and the orbital eccentricity. The last two columns report the total number and the total mass of the of simulated binaries, respectively. †The ICs for such models are under-sampled, the actual number of simulated systems and their total mass is reported in parentheses.

Input catalogs

Costa et al. (2023, [54]) built 13 SEVN input catalogs by varying the aforementioned distributions of the IMF, q, P, and e. For each of these catalogs they considered the metallicity $Z = 10^{-11}$. They set the total number of generated binaries to obtain 10^7 binaries in the high-mass regime ($M_{ZAMS,2} \geq 10\mathrm{M}_\odot$, and $M_{ZAMS,1} \geq 10\mathrm{M}_\odot$ by construction). For the models that draw the primary mass from K01 and L98, they limited the total number of generated binaries to 2×10^7 (consisting of 10^7 binaries in the high and low-mass range, respectively). As a consequence, the low-mass regime ($M_{ZAMS,2} \leq 10\mathrm{M}_\odot$) is under-sampled by a factor of $\sim 4-5$ for K01 and $\lesssim 1.2$ for L98. We take into account the incomplete sampling of the initial conditions by performing an a posteriori oversampling of the simulated binaries with $M_{ZAMS,2} \leq 10\mathrm{M}_\odot$. This ensures a good sampling of the high-mass regime and reduces stochastic fluctuations.

Table 6.2 lists the properties of our input catalogs. We label our input catalogs by taking the IMF name and adding a number that indicates the distribution of mass ratios, periods, and

eccentricities. Therefore, the LOG, KRO, LAR, TOP and PAR catalogs adopt the flat-in-log, K01, L98, top-heavy, and P23 IMF, respectively.
In all our models but LOG3 (Table 6.2), the ZAMS mass of the primary star $M_{ZAMS,1}$ is randomly sampled in the range $[5,\ 550]\mathrm{M}_{\odot}$, according to one of the five aforementioned distributions. The ZAMS mass of the secondary star ($M_{ZAMS,2}$) is then sampled based on the mass ratio distributions above-mentioned. The secondary mass can be as low as $2.2\mathrm{M}_{\odot}$.
In model LOG3, instead the entire IMF is sampled in the range $M_{ZAMS} \in [5,\ 550]\mathrm{M}_{\odot}$, according to the LOG distribution. The generated stellar masses are then randomly paired. The primary (secondary) star is thus the component with the higher (lower) initial mass.

6.2.2 Results

SEVN results

In Table 6.3 we report the results of the data analysis performed on the SEVN output. In the first column are reported all the models mentioned in Table 6.2, while in the second and third column we show PISNe and PPISNe rates. We notice that the values for KRO and LAR catalogs are substantially lower with respect to the TOP and PAR. Indeed the former are based on IMFs that favor low mass stars, in contrast to the latter. The flat-in-log distribution is instead in between these two regimes.Furthermore the differences arising within each model, with the same IMF, come from the different combination of models adopted for q, P and e.
Another consequence of the different IMFs adopted is the different occurrence of PISNe with respect to PPISNe for each model. In particular if the IMF favor more massive stars we register an higher rate of PISNe while, in the opposite cases, PPISNe are more numerous (as seen also in Section 6.1, where indeed stars follow a Kroupa IMF). In this case LOG model register analogous occurrences for PISNe and PPISNe.
Analogously to what done in Section 6.1, we evaluate the impact of mergers on the occurrence of pair-creation instability events. For this reason we report, in columns 4 and 5 of Table 6.3, the rates of PISNe and PPISNe occurring after a merger with respect to the total number of PISNe and PPISNe. Moreover we show in column 6 the merger rates with respect to the total number of systems. We notice that, for some models (e.g. LOG1, LOG3, LOG4, KRO1, LAR1, TOP1, PAR1), mergers are by far more common with respect to other models with the same IMF. This can be explained looking at the distribution of orbital periods of the aforementioned models. Indeed, in all the cases in matter, we adopted the S12 period model, that favor

Model	PISN rate (%)	PPISN rate (%)	rate PISN after merger (%)	rate PPISN after merger (%)	merger rate (%)
LOG1	13.59	13.22	32.24	18.12	31.25
LOG2	14.96	14.69	0.51	0.15	1.74
LOG3	17.46	14.02	42.94	23.99	45.58
LOG4	13.56	13.18	43.78	28.92	40.22
LOG5	14.35	14.49	0.49	0.13	1.69
KRO1	1.80	3.44	44.71	27.13	7.33
KRO5	1.70	3.45	0.76	0.28	0.10
LAR1	3.73	6.67	43.78	25.83	16.17
LAR5	3.49	6.69	0.70	0.26	0.29
TOP1	19.91	12.91	24.68	12.69	56.26
TOP5	22.33	16.20	0.41	0.06	4.57
PAR1	29.75	22.90	32.72	13.70	44.37
PAR5	27.42	23.94	0.46	0.08	1.63

Table 6.3: Column 1 contains the model for Pop. III initial conditions. Column 2 and 3 contain PISNe and PPISNe rates with respect the total number of supernovae. Columns 4 and 5 contain respectively the rates of PISNe and PPISNe occurring after a merger events with respect to the total number of PISNe and PPISNe. Column 6 contains the merger rate with respect the total number of system in each model.

short periods with respect to SB13. Shorter periods, because of the third Kepler law, implies shorter semi-major axis. Therefore such systems are tightly bound and they are more suitable to experience a merger during their lifetime. This explains the different results for each model. The large amount of mergers impact also on the rate of pair instability events occurring after a merger. Indeed, if we have a large fraction of mergers, we expect that a large fraction of PISNe and PPISNe occur after it. This is exactly what we observe for models LOG1, LOG3, LOG4, KRO1, LAR1, TOP1, PAR1.

COSMORATE results

Based on the data analysis of SEVN output by Costa et al. (2023, [54]), we produced ICs suitable for COSMORATE. As previously done in Section 6.1.2, we created input files considering the total amount of PISNe/PPISNe and PISNe/PPISNe occurring after or before a merger. The substantial difference with the work shown in Section 6.1.2 consists in data driven prescription adopted to describe the evolution of SFRD and metallicity. Since now we are dealing with Pop. III stars the previous equations 5.8 and 5.9 do not hold anymore. Therefore we need new suitable descriptions of SFRD and metallicity evolution. Concerning the SFRD, we make use of the A-SLOTH model by Hartwig et al. (2022, [66]). It is the only semi-analytic model

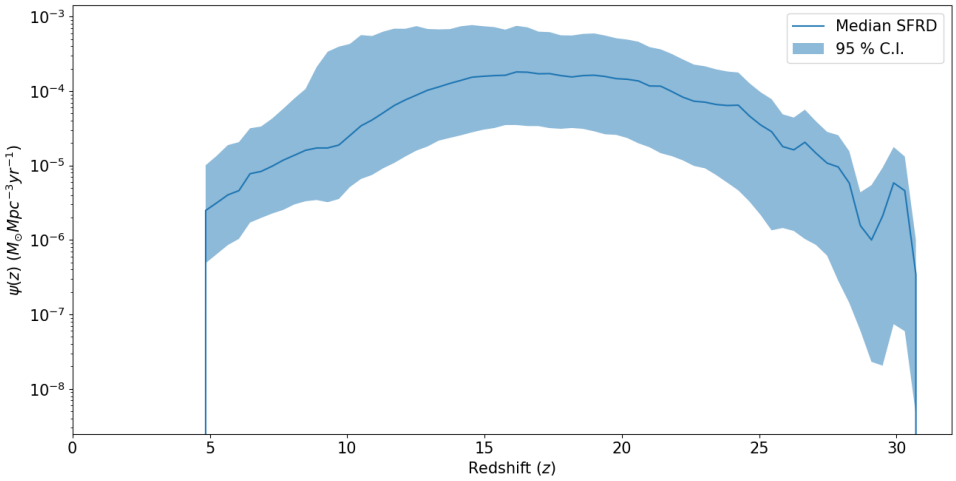

Figure 6.9: SFRD for A-SLOTH model. The blue area represents the 95% credible interval due to uncertainties in the unconstrained input parameters. The solid line is the median value of the SFRD.

that samples and traces individual Pop. III stars, and is calibrated on several observables from the local and high-redshift Universe – see Hartwig et al. (2022, [66]) and Uysal & Hartwig (2023, [67]). With A-SLOTH, it is possible to quantify the uncertainties in the SFRD that arise from unconstrained input parameters of the semi-analytic model. In particular through a Monte-Carlo technique is possible to provide > 5000 models, each with a slightly different SFRD. From these models, Santoliquido et al. (2023, [68]) extracted the central 95% credible interval of the SFRD. Figure 6.9 shows this 95% credible interval, which reflects uncertainties in the unconstrained input parameters.

With this SFRD we estimated the event rate density $\mathcal{R}$ of PISNe and PPISNe by means of Eq. 5.5. In this case $\psi(z)$ is the SFRD from A-SLOTH model and the distribution of metallicity at fixed formation redshift $p(z', Z)$ is not anymore a Gaussian distribution like in Section 6.1.2. Indeed since we model Pop. III stars with a single metallicity ($Z = 10^{11}$), we define $p(z', Z)$ as a delta function for Pop. III stars, different from zero only if $Z = 10^{11}$. Concerning the PISN/PPISN efficiency $\eta(Z)$ in Eq. 5.7, we assume that the binary fraction is $f_{bin} = 1$, and we do not apply any correction f_{IMF} for not sampling stars with mass $< 5 M_\odot$. We make this simplifying assumption because we do not know the minimum mass and binary fraction of Pop. III stars.

With the aforementioned procedure we estimated the event rate density for the total amount of PISNe and PPISNe found for each Pop. III model. The results are shown in Figure 6.10. From here we can observe that all rate densities have an analogous trend since they depend from

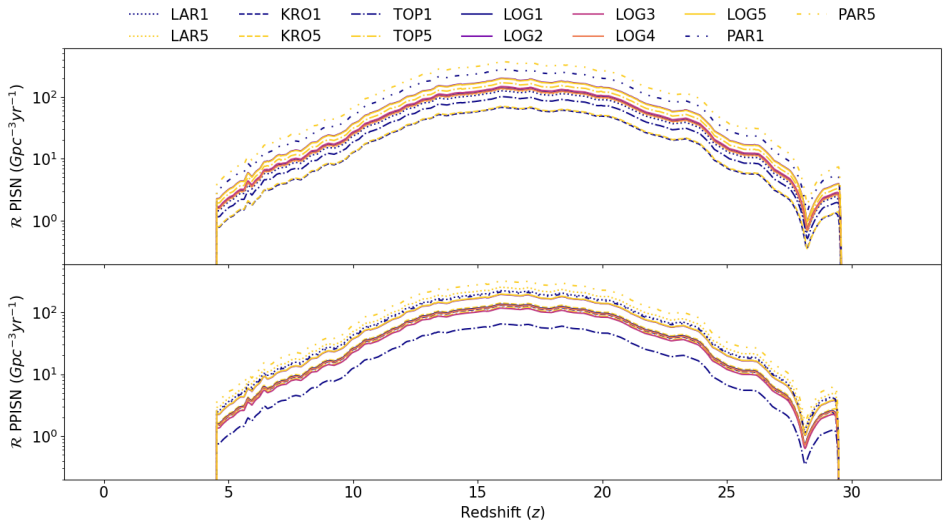

Figure 6.10: PISNe and PPISNe event rate density for each of the Pop. III model mentioned in Table 6.2.

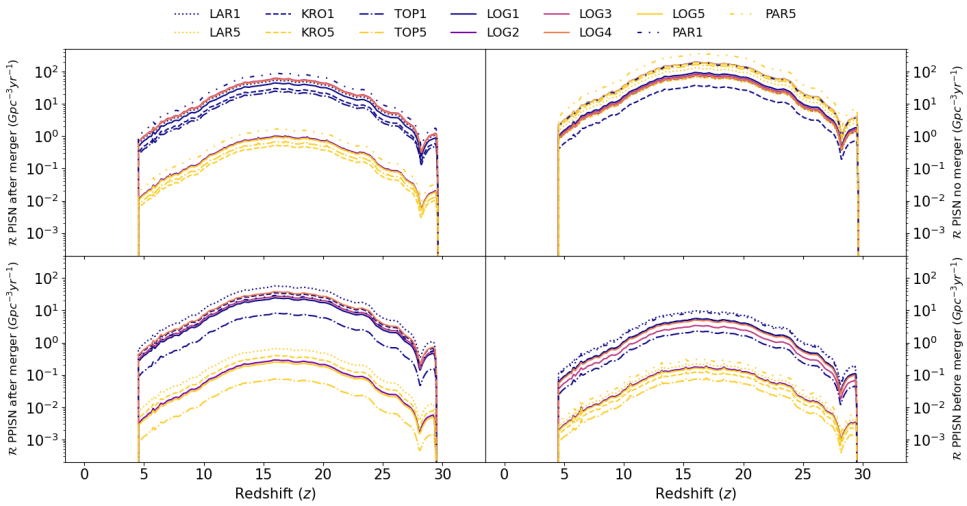

Figure 6.11: Rate density evolution of PISNe and PPISNe occurred after a binary merger and, before a merger for PPISNe and with no merger for PISNe, for each model in Table 6.2.

the same SFRD. Furthermore the most top-heavy models (PAR, TOP, LOG) reach, for both PISNe and PPISNe, rate densities even higher than 100 $\mathrm{Gpc}^{-3}\ \mathrm{yr}^{-1}$.

We also evaluated the event rate densities of PISNe and PPISNe occurred after a binary merger and, before a merger for PPISNe and with no merger for PISNe. The results are shown in Figure 6.11. Differently from Section 6.1.2, here we see that, in particular for PISNe, the rate densities for events occurring before and after a merger are comparable. This effect is probably due to the low metallicity ($Z = 10^{-11}$) and the fact that most of the IMFs adopted are more

top-heavy than the Kroupa previously used. In a population with these characteristics, stars have an high chance to undergo PISN/PPISN with no need of a previous binary merger.

7 Conclusion

In this work, we investigated the occurrence of pair-creation instability processes within stellar populations. We analysed sets of stellar populations with different characteristics, including effects induced by the cosmological evolution of the Universe.
By means of the population synthesis code SEVN [35, 36, 27], we evolved several SSPs and BSPs characterized by the same Kroupa IMF but different metallicities. We found rates of occurrence of PISNe and PPISNe with particular interest on the effects induced by metallicity Z and binary evolution events, e.g. mergers.
Increasing Z, also the mass loss rate increases ending up with stars, in advanced evolutionary stages, not sufficiently massive to be in the pair instability window.
Merger events dramatically change the evolutionary path of stellar systems. They can lead to the formation of stars that can experience PISN/PPISN, even if the progenitor stars, as single stars, were not sufficiently massive. Therefore the rate of production of PISNe and PPISNe, for these kind of populations, is always higher in BSP with respect to SSP.
The rates we found for PISNe seems to be partially in agreement with the constraints set by Takahashi (2018, [16]) and Moriya et al. (2021, [17]) mentioned in Chapter 2. Indeed, the rates in SSPs agree with the relative rate with CCSN of $0.01-0.1\%$, with variations depending on the metallicity. Instead concerning BSP, as aforementioned, rates are substantially higher reaching values of $1-2\%$. These last estimates resemble the values based on conventional stellar evolution simulations for the Salpeter IMF considering the initial mass range of PISNe of $140-260 M_{\odot}$.

Using the code COSMORATE [51, 52] we then evaluated the rate density of PISNe and PPSINe throughout cosmological epochs. We found the evolution of rate density with respect to the cosmological redshift z, assuming pre-computed expressions for SFRD and metallicity evolution. We found that the rate density of both PISNe and PPISNe reach a peak around $z \sim 2$, when the cosmic star formation rate density was at its maximum. In the local Universe we found rate densities of PISNe and PPSINe to be around 10^2 Gpc^{-3} yr^{-1} and 10^3 Gpc^{-3} yr^{-1} respectively. These values, in particular the one of PISNe, are in agreement with the constraints from Moriya et al. (2021, [17]).

We eventually analysed the SEVN outcome from Pop. III binaries simulations by Costa et al. (2023, [54]). Several models have been implemented to describe the possible evolution of this kind of stars. All of them are very metal poor ($Z = 10^{-11}$) and differ each other in binary properties and IMF. For instance the KRO model adopt a Kroupa IMF. Indeed, if we take into account the wider mass range here explored, we register similar PISNe and PPISNe rates with respect the simulations performed by us. Other models like LOG, TOP and PAR instead involve IMFs that are more top-heavy with respect to KRO and LAR models. For them, in fact, we found extensively larger PISNe/PPISNe rates reaching also values of $\sim 20 - 30\%$ with respect the total number of supernovae. Furthermore, by means of COSMORATE, for top-heavy models we found PISNe and PPISNe rate densities exceeding 100 Gpc^{-3} yr^{-1}. This indicates that, if Pop. III stars lose a negligible fraction of their mass via stellar winds and follow a top-heavy mass function, one of their main evolutionary channels leads them to explode as PISNe or PPISNe. Therefore, our calculations sugest that at high redshift PISNe and PPSINe were far more frequent than in the local Universe.

One of the major sources of uncertainty for our work is represented by stellar spins. Indeed, in our calculations, we neglected stellar rotation, albeit it can play a fundamental role in stellar evolution and final fate. Pop. III stars, in particular, might be fast spinning - see Yoon et al. (2012, [69]); Choplin et al. (2019, [70]). According to Tanikawa et al. (2021, [65]), we can have a glimpse of what happens to fast-spinning stars by considering the evolution of pure-helium stars. In fact, fast spinning stars at low metallicity effectively evolve toward chemically homogeneous evolution - see e.g., Marchant et al. (2016, [71]); du Buisson et al. (2020, [72]); Riley et al. (2021, [73]). Therefore it could be interesting to evolve and analyse populations of pure-helium stars, as a proxy for chemically homogeneous evolution, to get an idea of how fast-spinning stars evolve.

References

[1] T. Abel, G. L. Bryan, and M. L. Norman, "The formation and fragmentation of primordial molecular clouds," *The Astrophysical Journal*, vol. 540, no. 1, pp. 39–44, sep 2000. [Online]. Available: https://doi.org/10.1086%2F309295

[2] F. Nakamura and M. Umemura, "On the initial mass function of population III stars," *The Astrophysical Journal*, vol. 548, no. 1, pp. 19–32, feb 2001. [Online]. Available: https://doi.org/10.1086%2F318663

[3] V. Bromm, N. Yoshida, L. Hernquist, and C. F. McKee, "The formation of the first stars and galaxies," *Nature*, vol. 459, no. 7243, pp. 49–54, may 2009. [Online]. Available: https://doi.org/10.1038%2Fnature07990

[4] J. S. Vink, A. de Koter, and H. J. G. L. M. Lamers, "Mass-loss predictions for o and b stars as a function of metallicity," *Astronomy & Astrophysics*, vol. 369, no. 2, pp. 574–588, apr 2001. [Online]. Available: https://doi.org/10.1051%2F0004-6361%3A20010127

[5] S. E. Woosley, A. Heger, and T. A. Weaver, "The evolution and explosion of massive stars," *Rev. Mod. Phys.*, vol. 74, pp. 1015–1071, Nov 2002. [Online]. Available: https://link.aps.org/doi/10.1103/RevModPhys.74.1015

[6] R. B. Stothers, "Criterion for the dynamical stability of a non-adiabatic spherical self-gravitating body," *Monthly Notices of the Royal Astronomical Society*, vol. 305, no. 2, pp. 365–372, 05 1999. [Online]. Available: https://doi.org/10.1046/j.1365-8711.1999.02444.x

[7] G. Costa, A. Bressan, M. Mapelli, P. Marigo, G. Iorio, and M. Spera, "Formation of gw190521 from stellar evolution: the impact of the hydrogen-rich envelope, dredge-up, and 12c(α, γ)16o rate on the pair-instability black hole mass gap," *Monthly Notices of the Royal Astronomical Society*, vol. 501, no. 3, p. 4514–4533, Dec. 2020. [Online]. Available: http://dx.doi.org/10.1093/mnras/staa3916

[8] S. E. Woosley, S. Blinnikov, and A. Heger, "Pulsational pair instability as an explanation for the most luminous supernovae," *Nature*, vol. 450, no. 7168, pp. 390–392, nov 2007. [Online]. Available: https://doi.org/10.1038%2Fnature06333

[9] J. Bond, W. D. Arnett, and B. J. Carr, "The evolution and fate of very massive objects," *Astrophysical Journal*, vol. 280, pp. 827–847, may 1984.

[10] P. A. Crowther, O. Schnurr, R. Hirschi, N. Yusof, R. J. Parker, S. P. Goodwin, and H. A. Kassim, "The R136 star cluster hosts several stars whose individual masses greatly exceed the accepted 150 M$\odot$ stellar mass limit," *Monthly Notices of the Royal Astronomical Society*, vol. 408, no. 2, pp. 731–751, 07 2010. [Online]. Available: https://doi.org/10.1111/j.1365-2966.2010.17167.x

[11] A. Kozyreva, "Pair instability supernovae: Evolution, explosion, nucleosynthesis," Ph.D. dissertation, University of Bonn, 2014.

[12] N. Smith, W. Li, R. J. Foley, J. C. Wheeler, D. Pooley, R. Chornock, A. V. Filippenko, J. M. Silverman, R. Quimby, J. S. Bloom, and C. Hansen, "SN 2006gy: Discovery of the most luminous supernova ever recorded, powered by the death of an extremely massive star like η carinae," *The Astrophysical Journal*, vol. 666, no. 2, pp. 1116–1128, sep 2007. [Online]. Available: https://doi.org/10.1086%2F519949

[13] A. Gal-Yam, P. Mazzali, E. O. Ofek, P. E. Nugent, S. R. Kulkarni, M. M. Kasliwal, R. M. Quimby, A. V. Filippenko, S. B. Cenko, R. Chornock, R. Waldman, D. Kasen, M. Sullivan, E. C. Beshore, A. J. Drake, R. C. Thomas, J. S. Bloom, D. Poznanski, A. A. Miller, R. J. Foley, J. M. Silverman, I. Arcavi, R. S. Ellis, and J. Deng, "Supernova 2007bi as a pair-instability explosion," *Nature*, vol. 462, no. 7273, pp. 624–627, dec 2009. [Online]. Available: https://doi.org/10.1038%2Fnature08579

[14] A. Kozyreva, S.-C. Yoon, and N. Langer, "Explosion and nucleosynthesis of low-redshift pair-instability supernovae," *Astronomy & Astrophysics*, vol. 566, p. A146, jun 2014. [Online]. Available: https://doi.org/10.1051%2F0004-6361%2F201423641

[15] I. Arcavi, D. A. Howell, D. Kasen, L. Bildsten, G. Hosseinzadeh, C. McCully, Z. C. Wong, S. R. Katz, A. Gal-Yam, J. Sollerman, F. Taddia, G. Leloudas, C. Fremling, P. E. Nugent, A. Horesh, K. Mooley, C. Rumsey, S. B. Cenko, M. L. Graham, D. A. Perley, E. Nakar, N. J. Shaviv, O. Bromberg, K. J. Shen, E. O. Ofek,

Y. Cao, X. Wang, F. Huang, L. Rui, T. Zhang, W. Li, Z. Li, J. Zhang, S. Valenti, D. Guevel, B. Shappee, C. S. Kochanek, T. W.-S. Holoien, A. V. Filippenko, R. Fender, A. Nyholm, O. Yaron, M. M. Kasliwal, M. Sullivan, N. Blagorodnova, R. S. Walters, R. Lunnan, D. Khazov, I. Andreoni, R. R. Laher, N. Konidaris, P. Wozniak, and B. Bue, "Energetic eruptions leading to a peculiar hydrogen-rich explosion of a massive star," *Nature*, vol. 551, no. 7679, pp. 210–213, nov 2017. [Online]. Available: https://doi.org/10.1038%2Fnature24030

[16] K. Takahashi, "The low detection rate of pair–instability supernovae and the effect of the core carbon fraction," *The Astrophysical Journal*, vol. 863, no. 2, p. 153, aug 2018. [Online]. Available: https://doi.org/10.3847%2F1538-4357%2Faad2d2

[17] T. J. Moriya, J. an Jiang, N. Yasuda, M. Kokubo, K. Kawana, K. Maeda, Y.-C. Pan, R. M. Quimby, N. Suzuki, I. Takahashi, M. Tanaka, N. Tominaga, K. Nomoto, J. Cooke, L. Galbany, S. González-Gaitán, C.-H. Lee, and G. Pignata, "Constraints on the rate of supernovae lasting for more than a year from subaru/hyper suprime-cam," *The Astrophysical Journal*, vol. 908, no. 2, p. 249, feb 2021. [Online]. Available: https://doi.org/10.3847%2F1538-4357%2Fabcfc0

[18] Philipp Podsiadlowski. The evolution of binary systems. [Online]. Available: https://www-astro.physics.ox.ac.uk/~podsi/binaries.pdf

[19] A. Duquennoy and M. Mayor, "Multiplicity among solar type stars in the solar neighbourhood - part two - distribution of the orbital elements in an unbiased sample," *Astronomy and Astrophysics*, aug 1991.

[20] H. A. Kobulnicky and C. L. Fryer, "A new look at the binary characteristics of massive stars," *The Astrophysical Journal*, pp. 747–765, nov 2007.

[21] P. P. Eggleton, "Approximations to the radii of roche lobes," *Astrophysical Journal*, pp. 368–369, may 1983.

[22] D. Bhattacharya and E. P. J. van den Heuvel, "Formation and evolution of binary and millisecond radio pulsars," *Physics Reports*, pp. 1–124, 1991.

[23] M. Mapelli, "Formation channels of single and binary stellar-mass black holes," in *Handbook of Gravitational Wave Astronomy*. Springer Singapore, 2021, pp. 1–65. [Online]. Available: https://doi.org/10.1007%2F978-981-15-4702-7_16-1

[24] H. Sana, S. E. de Mink, A. de Koter, N. Langer, C. J. Evans, M. Gieles, E. Gosset, R. G. Izzard, J.-B. L. Bouquin, and F. R. N. Schneider, "Binary interaction dominates the evolution of massive stars," *Science*, vol. 337, no. 6093, pp. 444–446, jul 2012. [Online]. Available: https://doi.org/10.1126%2Fscience.1223344

[25] J. R. Hurley, O. R. Pols, and C. A. Tout, "Comprehensive analytic formulae for stellar evolution as a function of mass and metallicity," *Monthly Notices of the Royal Astronomical Society*, vol. 315, no. 3, pp. 543–569, 07 2000. [Online]. Available: https://doi.org/10.1046/j.1365-8711.2000.03426.x

[26] J. R. Hurley, C. A. Tout, and O. R. Pols, "Evolution of binary stars and the effect of tides on binary populations," *Monthly Notices of the Royal Astronomical Society*, vol. 329, no. 4, pp. 897–928, 02 2002. [Online]. Available: https://doi.org/10.1046/j.1365-8711.2002.05038.x

[27] G. Iorio, M. Mapelli, G. Costa, M. Spera, G. J. Escobar, C. Sgalletta, A. A. Trani, E. Korb, F. Santoliquido, M. Dall'Amico, N. Gaspari, and A. Bressan, "Compact object mergers: exploring uncertainties from stellar and binary evolution with sevn," *Monthly Notices of the Royal Astronomical Society*, vol. 524, no. 1, pp. 426–470, jun 2023. [Online]. Available: https://doi.org/10.1093%2Fmnras%2Fstad1630

[28] O. R. Pols, K.-P. Schröder, J. R. Hurley, C. A. Tout, and P. P. Eggleton, "Stellar evolution models for Z = 0.0001 to 0.03," *Monthly Notices of the Royal Astronomical Society*, vol. 298, no. 2, pp. 525–536, 08 1998. [Online]. Available: https://doi.org/10.1046/j.1365-8711.1998.01658.x

[29] J. J. Eldridge and E. R. Stanway, "bpass predictions for binary black hole mergers," *Monthly Notices of the Royal Astronomical Society*, vol. 462, no. 3, pp. 3302–3313, 07 2016. [Online]. Available: https://doi.org/10.1093/mnras/stw1772

[30] B. Paxton, L. Bildsten, A. Dotter, F. Herwig, P. Lesaffre, and F. Timmes, "Modules for experiments in stellar astrophysics (mesa)," *The Astrophysical Journal Supplement Series*, vol. 192, no. 1, p. 3, dec 2010. [Online]. Available: https://dx.doi.org/10.1088/0067-0049/192/1/3

[31] M. U. Kruckow, T. M. Tauris, N. Langer, M. Kramer, and R. G. Izzard, "Progenitors of gravitational wave mergers: binary evolution with the stellar grid-based code

ComBinE," *Monthly Notices of the Royal Astronomical Society*, vol. 481, no. 2, pp. 1908–1949, 08 2018. [Online]. Available: https://doi.org/10.1093/mnras/sty2190

[32] P. Agrawal, J. Hurley, S. Stevenson, D. Szécsi, and C. Flynn, "The fates of massive stars: exploring uncertainties in stellar evolution with metisse," *Monthly Notices of the Royal Astronomical Society*, vol. 497, no. 4, pp. 4549–4564, 08 2020. [Online]. Available: https://doi.org/10.1093/mnras/staa2264

[33] T. Fragos, J. J. Andrews, S. S. Bavera, C. P. L. Berry, S. Coughlin, A. Dotter, P. Giri, V. Kalogera, A. Katsaggelos, K. Kovlakas, S. Lalvani, D. Misra, P. M. Srivastava, Y. Qin, K. A. Rocha, J. Romá n-Garza, J. G. Serra, P. Stahle, M. Sun, X. Teng, G. Trajcevski, N. H. Tran, Z. Xing, E. Zapartas, and M. Zevin, "POSYDON: A general-purpose population synthesis code with detailed binary-evolution simulations," *The Astrophysical Journal Supplement Series*, vol. 264, no. 2, p. 45, feb 2023. [Online]. Available: https://doi.org/10.3847%2F1538-4365%2Fac90c1

[34] M. Spera, M. Mapelli, and A. Bressan, "The mass spectrum of compact remnants from the parsec stellar evolution tracks," *Monthly Notices of the Royal Astronomical Society*, vol. 451, no. 4, pp. 4086–4103, 06 2015. [Online]. Available: https://doi.org/10.1093/mnras/stv1161

[35] M. Spera and M. Mapelli, "Very massive stars, pair-instability supernovae and intermediate-mass black holes with the sevn code," *Monthly Notices of the Royal Astronomical Society*, vol. 470, no. 4, pp. 4739–4749, 06 2017. [Online]. Available: https://doi.org/10.1093/mnras/stx1576

[36] M. Spera, M. Mapelli, N. Giacobbo, A. A. Trani, A. Bressan, and G. Costa, "Merging black hole binaries with the SEVN code," *Monthly Notices of the Royal Astronomical Society*, vol. 485, no. 1, pp. 889–907, feb 2019. [Online]. Available: https://doi.org/10.1093%2Fmnras%2Fstz359

[37] S. E. Woosley, "Pulsational pair-instability supernovae," *The Astrophysical Journal*, vol. 836, no. 2, p. 244, feb 2017. [Online]. Available: https://dx.doi.org/10.3847/1538-4357/836/2/244

[38] C. L. Fryer, K. Belczynski, G. Wiktorowicz, M. Dominik, V. Kalogera, and D. E. Holz, "Compact remnant mass function: Dependence on the explosion mechanism

and metallicity," *The Astrophysical Journal*, vol. 749, no. 1, p. 91, mar 2012. [Online]. Available: https://dx.doi.org/10.1088/0004-637X/749/1/91

[39] H. Bondi and F. Hoyle, "On the Mechanism of Accretion by Stars," *Monthly Notices of the Royal Astronomical Society*, vol. 104, no. 5, pp. 273–282, 10 1944. [Online]. Available: https://doi.org/10.1093/mnras/104.5.273

[40] Y. Bouffanais, M. Mapelli, F. Santoliquido, N. Giacobbo, G. Iorio, and G. Costa, "Constraining accretion efficiency in massive binary stars with LIGO –Virgo black holes," *Monthly Notices of the Royal Astronomical Society*, vol. 505, no. 3, pp. 3873–3882, 06 2021. [Online]. Available: https://doi.org/10.1093/mnras/stab1589

[41] P. Hut, "Tidal evolution in close binary systems." *Astronomy and Astrophysics*, pp. 126–140, June 1981.

[42] P. C. Peters, "Gravitational radiation and the motion of two point masses," *Phys. Rev.*, vol. 136, pp. B1224–B1232, Nov 1964. [Online]. Available: https://link.aps.org/doi/10.1103/PhysRev.136.B1224

[43] P. Madau and M. Dickinson, "Cosmic star-formation history," *Annual Review of Astronomy and Astrophysics*, vol. 52, no. 1, pp. 415–486, 2014. [Online]. Available: https://doi.org/10.1146/annurev-astro-081811-125615

[44] P. Madau, H. C. Ferguson, M. E. Dickinson, M. Giavalisco, C. C. Steidel, and A. Fruchter, "High-redshift galaxies in the hubble deep field: colour selection and star formation history to z 4," *Monthly Notices of the Royal Astronomical Society*, vol. 283, no. 4, pp. 1388–1404, dec 1996. [Online]. Available: https://doi.org/10.1093%2Fmnras%2F283.4.1388

[45] P. Madau, L. Pozzetti, and M. Dickinson, "The star formation history of field galaxies," *The Astrophysical Journal*, vol. 498, no. 1, pp. 106–116, may 1998. [Online]. Available: https://doi.org/10.1086%2F305523

[46] S. J. Lilly, O. L. Fè vre, F. Hammer, and D. Crampton, "The canada-france redshift survey: The luminosity density and star formation history of the universe to [ITAL]z[/ITAL] ∼ 1," *The Astrophysical Journal*, vol. 460, no. 1, mar 1996. [Online]. Available: https://doi.org/10.1086%2F309975

[47] J. X. Prochaska, E. Gawiser, A. M. Wolfe, S. Castro, and S. G. Djorgovski, "The age-metallicity relation of the universe in neutral gas: The first 100 damped ly systems," *The Astrophysical Journal*, vol. 595, no. 1, pp. L9–L12, aug 2003. [Online]. Available: https://doi.org/10.1086%2F378945

[48] V. P. Kulkarni, P. Khare, C. Peroux, D. G. York, J. T. Lauroesch, and J. D. Meiring, "The role of sub–damped lyα absorbers in the cosmic evolution of metals," *The Astrophysical Journal*, vol. 661, no. 1, pp. 88–94, may 2007. [Online]. Available: https://doi.org/10.1086%2F515430

[49] M. Rafelski, A. M. Wolfe, J. X. Prochaska, M. Neeleman, and A. J. Mendez, "Metallicity evolution of damped ly-α systems out to z $\sim$ 5," *The Astrophysical Journal*, vol. 755, no. 2, p. 89, jul 2012. [Online]. Available: https://doi.org/10.1088%2F0004-637x%2F755%2F2%2F89

[50] A. D. Cia, C. Ledoux, P. Petitjean, and S. Savaglio, "The cosmic evolution of dust-corrected metallicity in the neutral gas," *Astronomy & Astrophysics*, vol. 611, p. A76, mar 2018. [Online]. Available: https://doi.org/10.1051%2F0004-6361%2F201731970

[51] F. Santoliquido, M. Mapelli, Y. Bouffanais, N. Giacobbo, U. N. D. Carlo, S. Rastello, M. C. Artale, and A. Ballone, "The cosmic merger rate density evolution of compact binaries formed in young star clusters and in isolated binaries," *The Astrophysical Journal*, vol. 898, no. 2, p. 152, aug 2020. [Online]. Available: https://doi.org/10.3847%2F1538-4357%2Fab9b78

[52] F. Santoliquido, M. Mapelli, N. Giacobbo, Y. Bouffanais, and M. C. Artale, "The cosmic merger rate density of compact objects: impact of star formation, metallicity, initial mass function, and binary evolution," *Monthly Notices of the Royal Astronomical Society*, vol. 502, no. 4, pp. 4877–4889, feb 2021. [Online]. Available: https://doi.org/10.1093%2Fmnras%2Fstab280

[53] P. Madau and T. Fragos, "Radiation backgrounds at cosmic dawn: X-rays from compact binaries," *The Astrophysical Journal*, vol. 840, no. 1, p. 39, may 2017. [Online]. Available: https://doi.org/10.3847%2F1538-4357%2Faa6af9

[54] G. Costa, M. Mapelli, G. Iorio, F. Santoliquido, G. J. Escobar, R. S. Klessen, and A. Bressan, "Massive binary black holes from population II and III stars," *Monthly*

Notices of the Royal Astronomical Society, vol. 525, no. 2, pp. 2891–2906, aug 2023. [Online]. Available: https://doi.org/10.1093%2Fmnras%2Fstad2443

[55] N. Giacobbo. (2021) Ic4popsyn. [Online]. Available: https://github.com/GiacobboNicola/IC4popsyn

[56] M. Moe and R. D. Stefano, "Mind your p_s and q_s: The interrelation between period (p) and mass-ratio (q) distributions of binary stars," *The Astrophysical Journal Supplement Series*, vol. 230, no. 2, p. 15, jun 2017. [Online]. Available: https://doi.org/10.3847%2F1538-4365%2Faa6fb6

[57] P. Marigo, L. Girardi, C. Chiosi, and P. R. Wood, "Zero-metallicity stars: I. evolution at constant mass," *Astronomy & Astrophysics*, vol. 371, no. 1, p. 152–173, May 2001. [Online]. Available: http://dx.doi.org/10.1051/0004-6361:20010309

[58] L. J. Murphy, J. H. Groh, S. Ekström, G. Meynet, C. Pezzotti, C. Georgy, A. Choplin, P. Eggenberger, E. Farrell, L. Haemmerlé, R. Hirschi, A. Maeder, and S. Martinet, "Grids of stellar models with rotation – V. Models from 1.7 to 120 $M_\odot$ at zero metallicity," *Monthly Notices of the Royal Astronomical Society*, vol. 501, no. 2, pp. 2745–2763, 12 2020. [Online]. Available: https://doi.org/10.1093/mnras/staa3803

[59] P. Kroupa, "On the variation of the initial mass function," *Monthly Notices of the Royal Astronomical Society*, vol. 322, no. 2, pp. 231–246, 04 2001. [Online]. Available: https://doi.org/10.1046/j.1365-8711.2001.04022.x

[60] R. B. Larson, "Early star formation and the evolution of the stellar initial mass function in galaxies," *Monthly Notices of the Royal Astronomical Society*, vol. 301, no. 2, pp. 569–581, 12 1998. [Online]. Available: https://doi.org/10.1046/j.1365-8711.1998.02045.x

[61] J. Park, M. Ricotti, and K. Sugimura, "Population III star formation in an X-ray background: III. Periodic radiative feedback and luminosity induced by elliptical orbits," *Monthly Notices of the Royal Astronomical Society*, vol. 521, no. 4, pp. 5334–5353, 03 2023. [Online]. Available: https://doi.org/10.1093/mnras/stad895

[62] A. Stacy and V. Bromm, "Constraining the statistics of Population III binaries," *Monthly Notices of the Royal Astronomical Society*, vol. 433, no. 2, pp. 1094–1107, 06 2013. [Online]. Available: https://doi.org/10.1093/mnras/stt789

[63] T. Kinugawa, K. Inayoshi, K. Hotokezaka, D. Nakauchi, and T. Nakamura, "Possible indirect confirmation of the existence of Pop III massive stars by gravitational wave," *Monthly Notices of the Royal Astronomical Society*, vol. 442, no. 4, pp. 2963–2992, 06 2014. [Online]. Available: https://doi.org/10.1093/mnras/stu1022

[64] T. Hartwig, M. Volonteri, V. Bromm, R. S. Klessen, E. Barausse, M. Magg, and A. Stacy, "Gravitational waves from the remnants of the first stars," *Monthly Notices of the Royal Astronomical Society: Letters*, vol. 460, no. 1, pp. L74–L78, 04 2016. [Online]. Available: https://doi.org/10.1093/mnrasl/slw074

[65] A. Tanikawa, H. Susa, T. Yoshida, A. A. Trani, and T. Kinugawa, "Merger rate density of population iii binary black holes below, above, and in the pair-instability mass gap," *The Astrophysical Journal*, vol. 910, no. 1, p. 30, mar 2021. [Online]. Available: https://dx.doi.org/10.3847/1538-4357/abe40d

[66] T. Hartwig, M. Magg, L.-H. Chen, Y. Tarumi, V. Bromm, S. C. O. Glover, A. P. Ji, R. S. Klessen, M. A. Latif, M. Volonteri, and N. Yoshida, "Public release of a-sloth: Ancient stars and local observables by tracing halos," *The Astrophysical Journal*, vol. 936, no. 1, p. 45, aug 2022. [Online]. Available: https://dx.doi.org/10.3847/1538-4357/ac7150

[67] B. Uysal and T. Hartwig, "First estimate of the local value of the baryonic streaming velocity," *Monthly Notices of the Royal Astronomical Society*, vol. 520, no. 3, pp. 3229–3237, 02 2023. [Online]. Available: https://doi.org/10.1093/mnras/stad350

[68] F. Santoliquido, M. Mapelli, G. Iorio, G. Costa, S. C. O. Glover, T. Hartwig, R. S. Klessen, and L. Merli, "Binary black hole mergers from population iii stars: uncertainties from star formation and binary star properties," *Monthly Notices of the Royal Astronomical Society*, vol. 524, no. 1, p. 307–324, Jun. 2023. [Online]. Available: http://dx.doi.org/10.1093/mnras/stad1860

[69] Yoon, S.-C., Dierks, A., and Langer, N., "Evolution of massive population iii stars with rotation and magnetic fields," *A&A*, vol. 542, p. A113, 2012. [Online]. Available: https://doi.org/10.1051/0004-6361/201117769

[70] Choplin, Arthur, Tominaga, Nozomu, and Ishigaki, Miho N., "Inferring the velocity of early massive stars from the abundances of extremely metal-poor stars," *A&A*, vol. 632, p. A62, 2019. [Online]. Available: https://doi.org/10.1051/0004-6361/201936187

[71] Marchant, Pablo, Langer, Norbert, Podsiadlowski, Philipp, Tauris, Thomas M., and Moriya, Takashi J., "A new route towards merging massive black holes," *A&A*, vol. 588, p. A50, 2016. [Online]. Available: https://doi.org/10.1051/0004-6361/201628133

[72] L. du Buisson, P. Marchant, P. Podsiadlowski, C. Kobayashi, F. B. Abdalla, P. Taylor, I. Mandel, S. E. de Mink, T. J. Moriya, and N. Langer, "Cosmic rates of black hole mergers and pair-instability supernovae from chemically homogeneous binary evolution," *Monthly Notices of the Royal Astronomical Society*, vol. 499, no. 4, pp. 5941–5959, 10 2020. [Online]. Available: https://doi.org/10.1093/mnras/staa3225

[73] J. Riley, I. Mandel, P. Marchant, E. Butler, K. Nathaniel, C. Neijssel, S. Shortt, and A. Vigna-Gómez, "Chemically homogeneous evolution: a rapid population synthesis approach," *Monthly Notices of the Royal Astronomical Society*, vol. 505, no. 1, pp. 663–676, 05 2021. [Online]. Available: https://doi.org/10.1093/mnras/stab1291